

Chapter 1

Poroelastic natural coatings

that its surface should be as smooth

Nature is the source of all true knowledge. She has her own logic, her own laws, she has no effect without cause nor invention without necessity

- , Leonardo Da Vinci

1.1 Introduction to biomimetics

Usually when we are asked to imagine some "rapid" object as an airplane, a boat or a car, common sense leads us to think about it as smoothest as possible. However, if we look around, Nature seems not to agree with the previous statement. In fact most of the surfaces in Nature are not at all smooth, they almost always present more or less regular arrangement of discontinuities at various length scales. Since Nature had a very long time-span to optimize this kind of surfaces we can suppose that they are the best possible options. One should pinpoint that the non-smoothness of these surfaces can be connected to some other biological functions rather than pure fluid dynamic performance, and of course it can be the case.

An example of natural surface is the shark skin⁵; in figure 1.1 a segment of the skin is depicted, as it appears ~~when~~ under the microscope.

The enlargement shows that the surface is made up by a series of overlapped denticles, and experiments show that they can move and interact with the flow. This interaction is supposed to reduce the shark drag when swimming.

The shark "technology" has somehow been applied by Speedo®; which ha designed their famous swimming suits with a surface that mimics shark skin. Multiple swimmers happen to break several world records wearing this swimming suits. This controversial swimmers' performance was due to the fact that they compress the body giving the swimmer a more streamlined shape. Even though the company has publicized their product as if it was a synthetic shark skin, Oeffner and Lauder [110] have shown that the texture of such swimming suits is somehow different from the shark dermal structure. In their work

Were
(qui è un
ogni tanto)

the swimsuit compressed

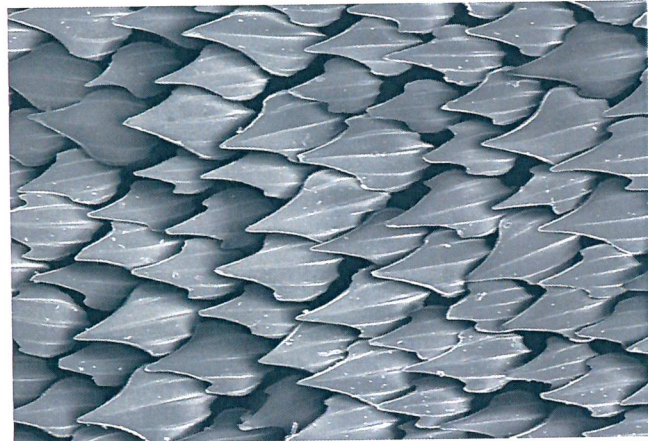


Figure 1.1: Microscope enlarged picture of the shark skin.

the authors have performed swimming experiment of a flat plate with different coatings and they did not find significant speed enhancement with a swimsuit-like surface, but the measurements with real shark skin on the contrary have demonstrated an appreciable improvement of the performance.

Poroelastic surfaces find also applications in aeroacoustics, as a matter of fact owls are well known for their particularly silent flight, especially in the high frequency spectrum. This characteristic is crucial for the owl in order to be able to capture its preys. Obviously it has inspired the scientific community to study their feathers configuration and shape.



Figure 1.2: Feathers on owl's wing. Left: trailing edge. Right: leading edge. The differences in shape and mechanical properties, as rigidity, between the leading and trailing edges is a consequence of the different flow regimes in the wing.

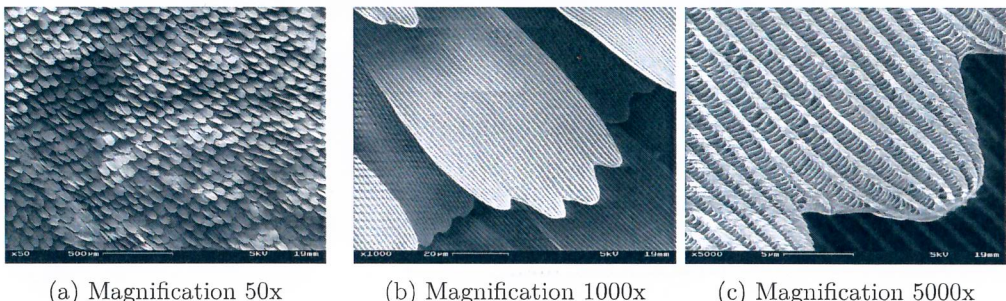
Several authors show promising results in characterizing the acoustic properties of the owl's skin and their physical mechanisms. In particular Lilley [90] presented three main characteristics of the owl, which can suppress its airborne noise: the feathers leading edge is shaped like a comb; the trailing edge forms a fringe and also multiple "filaments" in the

bottom surface of wing and legs.

Another example on the same topic is represented by Jaworski and Peake [78] who studied the acoustic scattering problem of a poroelastic half-plane encountering an incident plane wave. This configuration, a simplified owl's wing, explains how the properties of this surface can suppress the noise. They concluded that the combined effects of elasticity and porosity can produce a weaker noise amplification.

Recent computational simulations performed by Chen et al. [35] confirm that the leading edge shape of the feathers truly suppress noise and enhance the lift generation.

another peculiar example Bioinspired aerodynamic surfaces include another peculiar example in the butterflies' wings. In figure 1.3 the surface of a "Peacock butterfly" is enlarged in order to show the multiple scales involved; the wing structure present firstly a series of overlapped scales similar to the shark, but if we look closely we can observe that each scale has a complicate permeable structure.



(a) Magnification 50x

(b) Magnification 1000x

(c) Magnification 5000x

Figure 1.3: Particular of a Peacock butterfly wing, taken with a Scanning Electron Microscope. Images from wikipedia.org

Slegers et al. [135] have studied the effect of such porous structure on the performance in the flight of butterflies. Using cameras to measure the kinematics of their flight, they can measure their efficiency to "climb" (i.e. generate lift) and the stroke amplitude and frequency. The authors conclude that the porous structure of their wing gives a boost in climbing efficiency of 30%; this result clearly stresses out the importance of the poroelastic coating of the wings. Even though the butterfly flight aerodynamic is extremely complex, it is clear that the peculiar structure of the wing's surface is critical for their aerodynamic performances, as also Srygley and Thomas [137] confirms.

The last example concerns super-hydrophobic surfaces; these surfaces are water repellent, i.e. the water can slide over them with less resistance, resulting in very small values of wettability. This behavior is caused by the microscopic structure which forms the surface (see figure 1.4). In reality the rugosities are arranged in a quasi-regular way, in order to be able to capture air pockets that rest within the "valleys". These air inclusions provoke an effective slip at the air-liquid interface that causes the friction reduction; they also change

CHECK THE
REFERENCE
NUMBERS FOR
CONSISTENCY

such as that of the lotus leaf,
because of the surface's low wettability.

toughness elements

NA A COSTA
PARA REFERIMENTO?

the
the contact angle of droplets. Bottaro et al. [22] summarizes some of the above aspect and their applications.

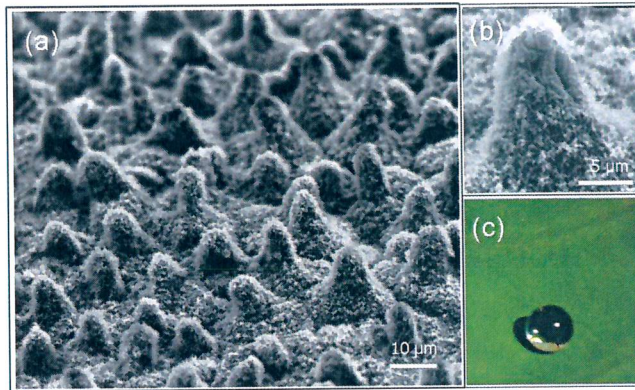


Figure 1.4: (a) Scanning electron microscopy (SEM) image showing the structure of lotus leaf, (b) higher order of magnification on the single protuberance forming the surface and (c) a water drop with high contact angle, attaining an almost spherical shape. Images from Stratakis et al. [138].

Interested readers can find more examples and broaden the above key aspect in Bhushan [19] and Tropea and Bleckmann [140].

1.2 Riblets and shark-skin surfaces

We have shown that natural surfaces can be an inspiration to find strategies in solving many problems concerning aerodynamics. In the following we especially focus on drag reduction.

It is known that the total drag contribution can be separated into different components and the classical decomposition is between viscous drag (sometimes referred to skin friction) and pressure drag.

$$\int_{A_\sigma} \left[\underbrace{(p\mathbf{I}) \cdot \mathbf{n}_\sigma}_{\text{pressure drag}} + \underbrace{\tau}_{\text{viscous drag}} \right] dA, \quad (1.1)$$

where the shear stress τ is defined as:

$$\tau = \mu (\nabla \mathbf{v} + \nabla^T \mathbf{v}) \cdot \mathbf{n}_\sigma \quad (\text{usually})$$

In (1.1) A_σ is the solid interface of some body where a no-slip condition is applied and \mathbf{n}_σ is its outward normal unit vector.

*W*indent — The shear stress in the turbulent case is defined as:

$$\tau_t = (\mu + \mu_t) [\nabla \bar{v} + \nabla^T \bar{v}] \cdot \mathbf{n}_\sigma \quad (1.2)$$

where μ_t is the turbulent viscosity and \bar{v} is the temporal average velocity. This section talks about the existing ways to reduce the viscous part of the drag working only on the surface texture.

1.2.1 Riblets

Most ~~of the~~ industrial applications involve turbulent flow, as a result, there is a lot of research that aims to reduce ~~the~~ skin friction in this regime. Table 6.3.1 in the book of McLean [98] includes a wide list of techniques already been proposed on the problem. As the same author pinpoints, the most effective and, probably the most practicable solution, is the surface texture known as ~~the~~ riblets. Riblets are alternating ridges aligned in the streamwise flow direction and regularly arranged, as figure 1.5 shows. These surfaces are capable to align the turbulent flow along the mean flow direction, smoothing the fluctuation~~s~~ of the crossflow in the viscous sublayer. The turbulent momentum transfer is reduced ~~and~~ as consequence of reducing these fluctuations close to the surface. In the same manner the surface experience ~~less~~ a lower skin friction.

The viscous drag reduction correlates well with the spacing between the ridges expressed in wall units, s^+ . The typical shape of the $\Delta\tau/\tau_0 - s^+$ relation is depicted in figure 1.6, where the vertical axis shows the drag reduction against ~~the~~ s^+ . This general shape of the curve, in which the skin friction decreases in certain range of spacing and then increase as the ridge spacing increases, is caused by a competition between the capacity of riblets to obstruct lateral fluid flow and the increase of penetration of high speed vortices inside this manufactured wall irregularity.

This last physical explanation of the riblets performances is presented in the schematics 1.7, where the gray areas show high skin-friction regions caused by the downwash motion generated by the near-wall vortices. It is clear that, when the riblets are too large, the vortices can penetrate inside the groove and ~~actually~~ increase the skin-friction, due to larger area exposed to the local velocity. On the contrary, when the riblets are smaller, the high speed vortex only hits the tip of the ridges, so only a small local area of the surface experiences high-shear stresses.

The slope m_s of the curve in figure 1.6 can be predicted by linear stability theory (either in laminar and turbulent cases changing the definition of base flow) or by means of empirical correlations García-Mayoral and Jiménez [57].

Computing the performance of such surfaces can be expensive, since the most reliable quantitative theory for such problems consist of direct numerical simulations (DNS) or experiments. However there is ~~only~~ one ~~more~~ theory, besides the already cited expensive ones, that uses the concept of *protrusion height*, shown in figure 1.5, to correlate the shape of these protrusions to the drag reduction (cf. Luchini et al. [91]). In this way the

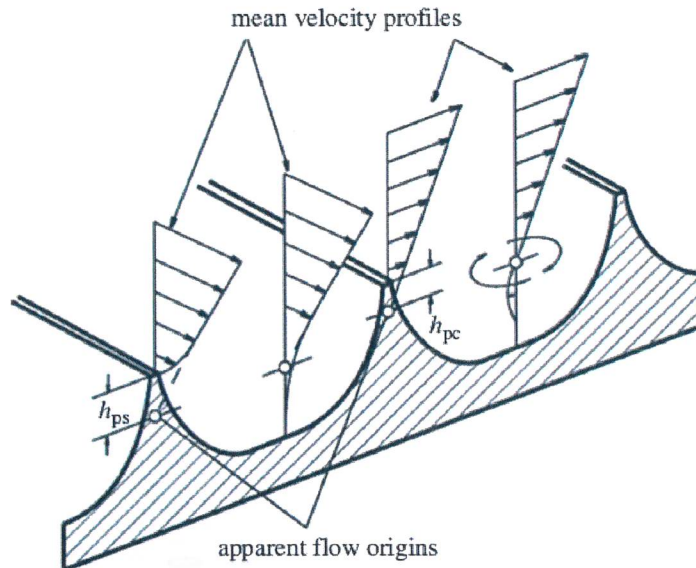


Figure 1.5: Schematics of the *protrusion height* concept. The mean velocity profiles for the stream-wise and crossflow velocities are shown. In presence of a ridge it is possible to extrapolate the point of zero velocity from the velocity gradient outside the riblet; finding respectively, the *streamwise protrusion height* h_{ps} and the *cross-flow protrusion height* h_{pc} . Image from Bechert et al. [16].

protrusion height is defined as the vertical distance between the riblet top ridge and the point of zero velocity, extrapolated from the constant velocity gradient outside above the protrusions. It appears that the difference of protrusion heights ($h_{ps} - h_{pc}$) correlates very well with the drag reduction. The two quantities can be computed with a simple Stokes problem over the local geometry of the grooves. The last result has been analyzed by Gomez-de Segura et al. [64] that propose an empirical law for the drag reduction, relating the previous protrusion heights with the permeability expressed in wall units:

$$-\Delta\tau/\tau_0 = DR \approx 0.04 \left(\sqrt{K_s^+} - \sqrt{K_c^+} \right), \quad (1.3)$$

where K_s^+ and K_c^+ are the streamwise and crossflow permeability tensor components. This law establishes a relation that help to estimate the drag reduction from a given geometry of the wall. The permeability tensor can be computed within the porous media homogenization approach as chapter 2 explains.

Another important characteristic of riblets ~~performance~~ is that they are robust in off-design conditions, such as in presence of yaw (misalignment between flow and riblets ridges)

Secondo me
questo per
re
tutto
(oppure
spiegato
molto
meglio!)

MA COSA C'ENTRA ??
NEL CASO DELLE RIBLETS
LA PARETE NON E'
POROSA, COME DEFINISCI LA
PERMEABILITA' ??

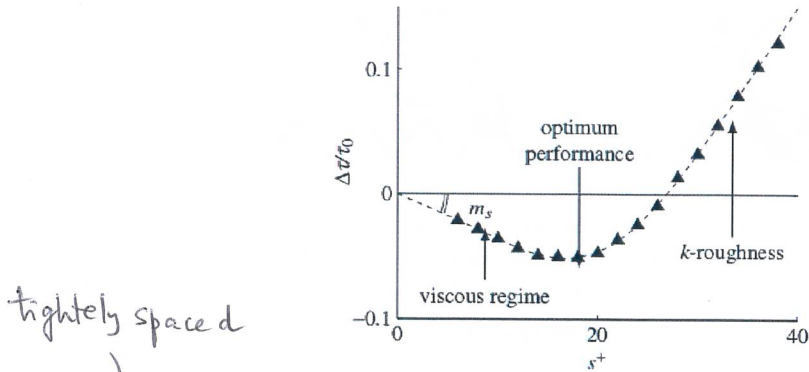


Figure 1.6: Example of drag reduction relation to the ridge spacing. The maximum performance is normally around $s^+ = 15$, the picture shows also that when the riblet are really tight one another the laminar case is retrieved. On the contrary when the riblets are far away one another their performance is comparable to rough plate case. Image from Jimenez et al. [79]. To is the wall stress in the core of a smooth flat plate.

and tip ridges erosion (García-Mayoral and Jiménez [56]).

Besides some very specific application such as sailing competitions (the hulls of the USA challengers in the America's Cup 1987 and 2010), the massive use of this technology is still in question. Producing such surfaces in a larger area, like the roof of a car or the wing of an airplane, can be an issue for a routine use because riblets size need to be very little to be effective. The riblets need also to be cleaned after each use otherwise some residue (like insect or vegetation) can modify the roughness of the surface and reduce their effectiveness.

Anyhow, riblets-like surface has been observed in nature for many years, for example Martin and Bhushan [95] found that skimmer birds (Rynchops) have riblets like grooves in their beak, since they fly with it under the water surface to catch fishes. However, as already introduced, the most clear example of such natural surfaces are shark skin.

1.2.2 Shark skin

In this review, Dean and Bhushan [43] present the status of the shape optimization that has been done on the riblets trying to mimic the typical sawtooth shape seen on shark skin, showing that improvements of such geometries over the classical ones has yet to be achieved. Shape optimization on riblets geometry has been studied, the findings show that just a few % can be improved on the base line geometry Bechert et al. [16].

There are, actually, some controversial results in literature stating that surfaces, with actual shark skin replica, can indeed increase drag. Boomsma and Sotiropoulos [21] per-

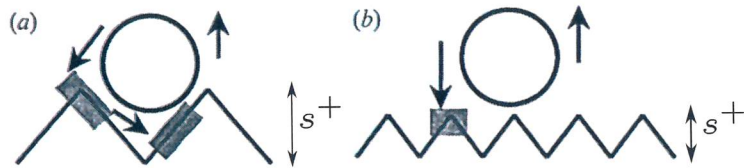


Figure 1.7: Two different sizes of riblets are shown when interacting with a sublayer vortex. In gray it is represented the area where friction is important. Clearly when both sizes are comparable the surface experience a larger friction and the performance is lowered. Image from Choi et al. [36].

These formed some simulations on actual shark skin denticles using the immersed boundary method. The authors simulate various arrangement of the denticles and they find that, in some configuration, the actual drag increase up to 40%. This can be a clue that the shark skin does not work with the same mechanism as riblets do.

hate *shown* *needed to* *during* Experiments on such geometries are available in literature (Bechert et al. [15]). The authors built a synthetic surface, made by artificial shark denticles posed on top of springs. They measure that even with the introduction of surface elasticity, the actual drag was increased. However, they pinpointed that the actual shark flow regime was not steady in the experiments that were performed, and they speculated that the excellent swimming performance of the shark comes from the separation control that flexible denticles can operate *increase in* the periodic oscillating flow that the swimming generates.

In addition an experiment using DPIV on a NACA profile covered with actual skin samples of "Isurus oxyrinchus" mako shark, has been performed by Lang et al. [87], confirming that the flexibility of sharks denticles act as a passive flow control in order to avoid early separation. In fact, the experiment had proven that for angles of attack larger than 15° the flow reversal was almost completely avoided. The same author noted that different geometries of the denticles can be found in various parts of the shark body, and these differences can be important since flow conditions can change from the head to the tail. Motta et al. [104] perform a detailed collection of flexibility and scale measurement of different shark species that can be valuable for future studies.

Again, swimming experiments from Oeffner and Lauder [110], who used a flat plate covered with real shark skin, confirmed the previous flow control mechanism. They had also made some conjectures about possible thrust enhancing, controlled by the same denticles, that can move away the leading edge vortex.

Also Itoh et al. [77] showed that movable rugosities can outperform riblets, the authors measured the drag reduction of a seal fur (that present fibrous movable surface) against a riblet surface in an experimental channel. Their results are shown in figure 1.8 in which it is visible that seal fur can outperform rigid riblet performance by 5% in a certain span of Reynolds number.

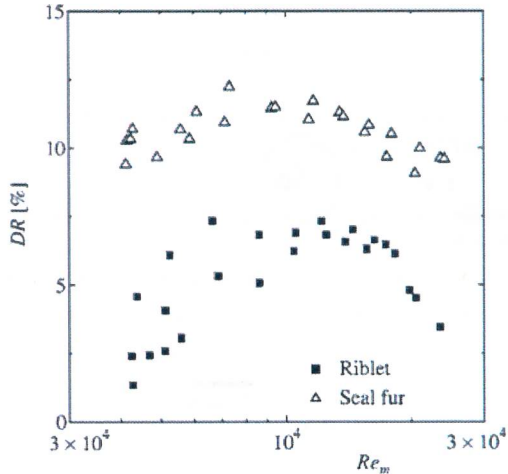


Figure 1.8: Performance comparison between a riblet surface against a seal fur. The drag reduction has been computed as: $DR\% = \frac{\Delta \tau}{\tau_0} \%$ Image from Itoh et al. [77].

Compliant surfaces can, in reality, move accordingly to the surface pressure gradients along the boundary layer and so respond to the pressure fluctuation over the surface itself. This mechanism is already known to be beneficial in delaying the transition to turbulence and many authors have presented theoretical and experimental evidence on the effectiveness of this solution (Carpenter [34], Bushnell et al. [29]).

In conclusion, we have seen that, in order to reduce turbulent skin-friction drag, riblets and natural surfaces use various mechanisms such as: sublayer vortices interaction, compliance and separation control. Such solutions have proven to be effective in various cases mostly related to the viscous component of the drag. In the next section we introduce another class of solutions that try to act mostly on the pressure component.

1.3 Permeable surfaces

As permeable surfaces we indicate permeable coatings that usually have ~~an important~~ ^{a significant} thickness; in contrast to riblets, in which the vertical extension outside the wall is limited. In this case the flow can penetrate deep into the porous surface and generate complex interaction mechanisms. The next sections presents an overview of the most notable applications of such permeable surfaces.

1.3.1 Bluff bodies

There is some experimental evidence that, ^{the} in laminar regime, generation of some *slip velocity* at the interface between the permeable surface and a fluid, can decrease the skin friction (Beavers and Joseph [14]). However, in the turbulent case it seems that the instabilities developing at the interface can cause an increase in drag up to 40% (Jimenez et al. [79]; Breugem et al. [23]); ^{these} mechanism is further explained in section 1.5. It is important to ~~observe~~ that the permeable surfaces cited in the above references are all rigid.

have

The pressure contribution to the drag is usually the most significant one in bluff bodies applications, and even in highly streamlined body it is around 10% of the total drag. Researchers tried to find a way to modify the pressure distribution around a bluff body to reduce the associated resistance, and also ~~damp~~ ⁵ the force oscillation on the body (drag and/or lift).

The pressure drag on a bluff body depends mostly on the difference between the low pressure on the rear part of the body, where there is usually a separated flow region, and the high pressure in the forward part. This idea is sketched in figure 1.9 where two different pressure distributions are shown; the black one represents the classical solid body, and the green one is the one with a porous layer at the back of the body.

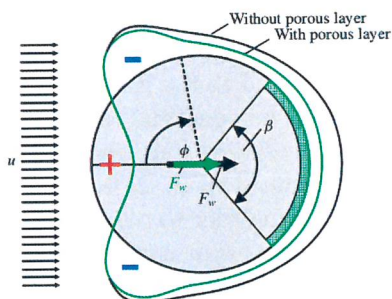


Figure 1.9: Diagram showing an example of angular pressure distribution around a cylinder for viscous flow. The black line is the case of a solid body, the green one is the modified pressure in presence of a porous layer at the rear part. Image from Klausmann and Ruck [81].

The favorable increase of ~~the~~ pressure in the rear point is due to the low speed laminar flow in the porous media that is ejected in the back region where separation takes place. Even in very high speed turbulent flow the fluid inside permeable surface exhibits a very high energy loss due to the strong dissipation that the medium provides, resulting in a low speed flow ejected downstream of the body.

The permeable interface, producing a slip velocity, can modify the boundary layer

that develops above it producing less shear and vorticity, modifying also the stability characteristics of the flow. The instability around a cylinder is due to the shear layer that forms in the top part of the body, when the flow starts to decelerate. This shear layer exhibits a Kelvin-Helmholtz-type instability that develops in the classical Von-Karman wake. *These* [26, 27]

~~This two hypothetical mechanisms has been tested using numerical simulation by multiple authors: Bruneau and Mortazavi [26], Bruneau and Mortazavi [27], Bhattacharyya and Singh [18], Naito and Fukagata [105] and Mimeau et al. [102]. These works studied the flow around some classical two dimensional bluff bodies (cylinder, square cylinder, Ahmed body section, 3D hemisphere) with the ~~add~~ of a porous layer.~~

These works show some very promising results, like: decrease of enstrophy, lower oscillations in lift ~~area~~, drag reduction, regularization of the wake and lower pressure gradients, even if the porous medium was rigid in the ~~the~~ case. An example of turbulent flow field downstream to a square cylinder is shown in figure 1.10; the picture ~~display~~ how the porous layer strongly regularize the wake.

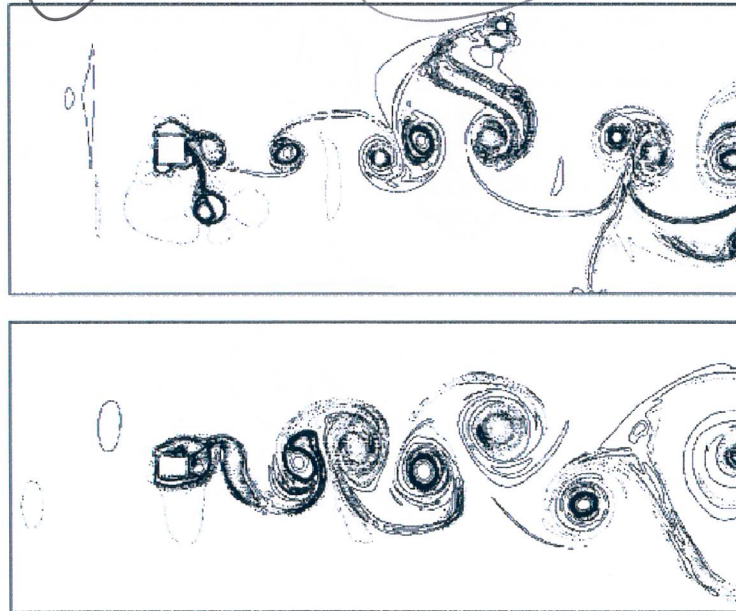


Figure 1.10: Square cylinder vorticity contour for $Re = 30000$. Top: solid case. Bottom: porous case with layer extension $h = 10\% D$.

The simulations performed by the authors above indicate that porous medium parameters, like the medium porosity or its vertical extension above the solid wall, have important effects on the results. The variety of results seems to agree (at least qualitatively) that

beyond

increasing the porous medium extension over a certain limit is not beneficial, and they also show that the porosity of the medium should not be excessive in order to be effective (high/medium porosities are the best).

However the above results should be taken with some care; only few cases are three-dimensional, they all use a modeling approach for the porous medium based on a simplified version of the VANS (Volume Average Navier-Stokes equations, see section 1.4.2), without performing any validation of the method. Sometimes they also use the equations outside their field of validity (there are some discussions in the scientific community about using the previous version of VANS equations for highly turbulent flows).

The lack of validation reflects the fact that reliable experiments of such porous coatings are almost non existent in literature. There is also some confusion in the community on how to compute forces on such bodies surrounded by a porous coating. These differences led some authors (Naito and Fukagata [105]) to over-estimate the forces and their predictions are not inline with the literature. Moreover Caltagirone [30], with some theoretical bases, establishes that the approach used by Bruneau and Mortazavi [26] is the correct one for that specific version of the VANS used by all the previous authors.

The approach of Favier et al. [49] differentiates itself from the previous approach that use the VANS equations. In fact the authors use a numerical method that includes the dynamics of a moving porous medium made of fibers at the back of a cylinder. Their results in a laminar flow case agree with the prediction of a stabilization of the wake and show some more realistic values of drag reduction, about 15%. However the difficulties in this approach lie in the medium dynamics, it introduce many mechanical parameters that are not easily identifiable for natural surfaces.

A similar model has been used by Venkataraman and Bottaro [142], in which they applied a movable porous coating in the upper part of NACA airfoil. In this case the synchronization between the oscillations of the structures and the natural frequency of the fluid is responsible for the pressure distribution modification. They have shown the robustness of this solution in a wide range of angles of attack, and, in the best case, they have found some lift enhancement and a drag reduction around 10%.

Later on Rosti et al. [128] worked on a similar configuration with only one movable flap on the low pressure side of the airfoil; the both numerical and experimental results qualitatively agree (on the flow mechanism) with the results in the complete porous case.

SHOW SOME RESULTS ON THE 3D SPHERE USING HOMOGENIZATION WHEN IT WILL BE PUBLISHED giuseppe ... [63]

The very few experiments in literature on this porous coatings show less promising results associated to drag reduction.

For example, Heenan and Morrison [71] perform an experiment in which they take a backward facing step with a porous insert in the re-circulation region. Their measurement shows a 13% decrease of the peak of pressure at the wall and a relocation of the detachment point further downstream. A maximum of 9% of drag reduction was measured. The effect of adding a porous surface in this case was to limit the pressure fluctuations that cause the

L'ARTICOLO
È STATO
INVIAUTO.
PUÒ
ESSERE
CITATO
come
"submitted".

To the best of

re-circulation bubble unsteadiness.

Later on Klausmann and Ruck [81] studied a 3D cylinder with a porous insert in the back (as in figure 1.9); the authors used a wind tunnel testing with pressure measurements around the body and particle image velocimetry (PIV) flow capture. Their results confirmed that the porous layer on the leeward side increased the pressure in that zone, causing a reduction of drag around 10% over various Reynolds number (in turbulence range). This last measurement was sensitive to the geometrical parameters of the medium as the position and its size. At our knowledge this is the first example of actual measurements of flow quantities using PIV, that can later be used to perform some validation on different numerical models. The above results are partially confirmed by a similar experimental analysis by Grizzetti et al. [68].

Some other experimental data can be found in the case of flow over aquatic canopies (Zhang and Nepf [160], Segalini et al. [130] and Hamed et al. [70]) even though the published data are limited and the experiments show the presence of a free surface that increase the difficulty of the problem and limit the possible use as a simple validation.

From this section the main physical mechanism related to permeable surfaces has been introduced. Even though the different approaches in literature seem to be discordant in the predicted values of some fundamental items such as the forces, a general trend on all data shows that porous coatings can be effectively used in many situations. It is clear that the scientific community needs much more experimental data in order to develop new and improved numerical and theoretical models for such permeable coatings.

1.3.2 Canopy flow

Another important class of flows over poroelastic carpets are the *canopy flows*, as named in literature. These type of problems involve flows over flexible slender structures such as trees and aquatic vegetation. The behavior of wind over plants is very important in a large variety of fields, like: the transport of substances as CO_2 and nutrients or preventing agricultural damage (wind-throw of crop fields); also some similarities with urban canopies can be found (Ghisalberti [59]).

The boundary layer profile over such canopies differs substantially from the rough wall one, as figure 1.11 shows. The vegetation resistance causes the creation of an inflection point in the mean velocity profile that leads to a mixing layer type of instability (Kelvin-Helmholtz instability) near the vegetation top. As a consequence of such instabilities Finnigan [51] indicated that the vegetation can heavily modify the turbulence spectra as a result of the interface instabilities and the coherent structures above it. The two pictures in figure 1.11 outline the above statements; the spectrum in case of canopy flow presents a larger peak in the frequency of the mixing layer instability, a steeper slope in the energy cascade part due to the larger dissipation inside the permeable layer and possible high frequency peaks associated to the swinging of the plants that can emit or absorb small scales vortices.

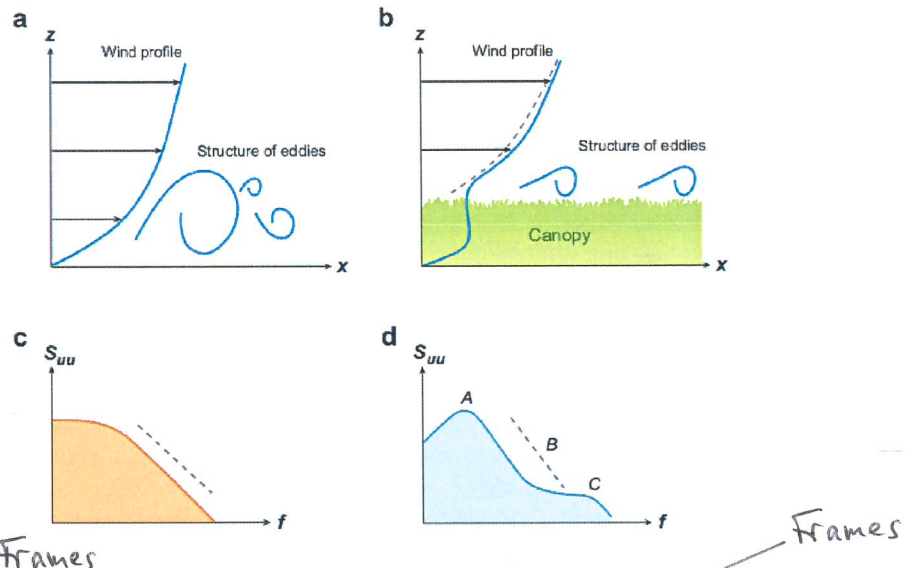


Figure 1.11: Figure a and b show respectively the schematics of the mean flow over a rough wall and a canopy flow; the difference in the eddy size is clear, also the inflection point in the canopy flow velocity profile is obvious. The figure c and d instead show the turbulent spectra for the two different flows above, in case of rough wall a Kolmogorov type of spectra can be retrieved, in case of canopy flow it is possible to see a larger peak in the frequency of the mixing layer instability, a steeper slope in the energy cascade part and high frequency peak at high frequencies. Image from De Langre [42].

Is it clear from literature that the dynamic of the permeable substrate made by vegetation is extremely important and should always be taken into account to fully generalize the physics in such problems involving moving canopies; Nepf [106] shows how the interface between aquatic plants and the free flow can be largely modified due to the movement of the fibers (most of the plants arm and branch can be viewed as fibers).

In order to discriminate the different behavior of the fibrous structure it is convenient to introduce some non-dimensional parameters used in fluid structure interaction problems:

$$m^* = \rho_\beta / \rho_\sigma, \quad C_Y = \rho_\beta U_\infty^2 s^3 / E, \quad s = H/d,$$

where ρ_β is the fluid phase density, ρ_σ is the solid phase density, U_∞ is a free-stream reference velocity, E is the Young modulus of the solid material, H is a reference length for the extension of the solid structure and d is a reference length for the thickness of the material. The first parameter is the *mass ratio* (m^*), the second is called *Cauchy number* (C_Y) and the last one is the *slenderness* (s) of the structure. The mass ratio ~~can be used to~~ ~~a measure of~~ the added mass effects caused by ~~the~~ solid inertia, however these effects are

usually negligible in case of fibrous permeable media. The Cauchy number defines the static deformation of a fiber caused by the fluid flow; when Cauchy number is greater than unity, important deformations are expected. This last parameter is extremely important since it controls a phenomenon called *reconfiguration* that leads to drag reduction (Gosselin and De Langre [66] and Alvarado et al. [4]). The reconfiguration can be defined as the capability of the structure to adopt a new shape when forced by a flow, usually it becomes more streamlined to reduce its exposed frontal area with the aim to reduce the total drag. When dealing with this phenomenon one should take into account ~~of~~ the frontal area A and the drag coefficient C_D as an ensemble, in order to avoid misinterpretation of the drag reduction; in figure 1.12 the ratio of the parameter AC_D has been represented for different natural structures against the Cauchy number and ~~is~~ it is evident that for a $C_Y > 1$ a drastic drag reduction can be observed.

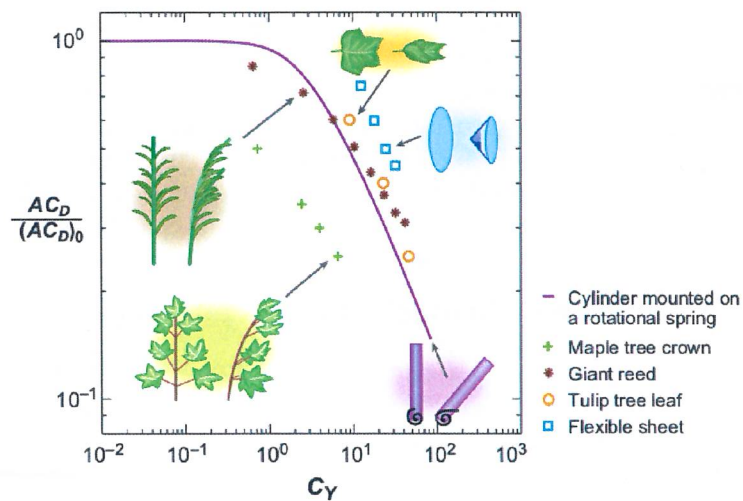


Figure 1.12: The effects of the Cauchy number C_Y on the drag reduction are presented in the figure. The drag reduction has been represented as the ratio between the frontal area A and the drag coefficient C_D at static condition (subscript 0) and the dynamic condition in dynamic conditions, divided by the same product under static conditions (subscript 0).

The overall reconfiguration of the permeable medium can lead to pressure recovery and a wake regularization when applied to a bluff body, as the experiments by Gosselin and De Langre [66] show.

Another important non-dimensional number is the *reduced velocity* (U_R), that can be derived from the previous ones:

$$U_R = \sqrt{C_Y s/m^*}$$

This number is used dealing with vortex induced vibration of slender structures; when it

is near ~~to~~ one, dynamical coupling between the fluid and the structure is expected, such as resonance or lock-in phenomena (self-excited vortex-induced vibrations accompanied by the synchronization of the frequency of vortex formation with the frequency of structure vibration).

Canopies can also help to prevent separation in presence of adverse pressure gradients. Belcher et al. [17] show an analysis of the flow over a hill covered with canopies using either numerical and experimental data; the authors show how the permeable layer can present a re-circulation region inside the canopy in the decreasing slope side of the hill. This zone move the separation away from the flow over the hill to the internal structure of the canopy.

It is important to ~~point~~ ^{out} that the above results are restricted to fibrous or slender structures and they cannot be extrapolated in general for different porous structure and shapes, even though similar mechanisms are expected.

The research on canopy flow embraces a wide range of configurations and this makes very difficult the comparison of the results since most of the authors use very different models in various regimes of velocities, using flexible structures with very different shapes. Even if experiments are easier to find, like Segalini et al. [130], Segalini et al. [131], Maza et al. [96], Barsu et al. [10] and Alvarado et al. [4], there is no quantitative mathematical model established for the fluid and structure equations and almost all models available rely on empirical correlations that fit the data in each different application.

1.4 Models for flows through porous surfaces

In this section we want to show some insight of the key characteristic that a model of flows through poroelastic layers should have. In order to be as clear as possible we have taken as example a very simple geometry to sketch the problem; the flow over a wall that includes ~~flexible~~ ~~multiple~~ filaments (in the hypothesis of highly packed fibers their whole totality can be treated like a porous medium). This simple geometrical configuration still has all the characteristic and difficulties of more interesting applications, such as a bluff body with a poroelastic layer.

The figure 1.13 shows a graphical ~~sketch~~ ^{representation} of such flow; the main fluid direction is aligned with the x_1 axis and the projection of velocity stream-wise component is shown in the plane $x_1 - x_3$. Such flow can bend the filaments that can show a more or less coherent response. The surface that envelops all the filaments lid (Γ) defines the limit between the ~~flow without obstacle~~ (Ω_f) and the one inside the poroelastic medium (Ω_p). Its projection is shown in the $x_1 - x_3$ plane.

In order to computationally solve this problem there are some key points to address:

- Length scales: the flow presents interaction at multiple scales. The flow can develop Kelvin–Helmholtz type instabilities on the interface ~~of size~~ and they can even penetrate inside the medium and brake up to very small scales eddies. In order

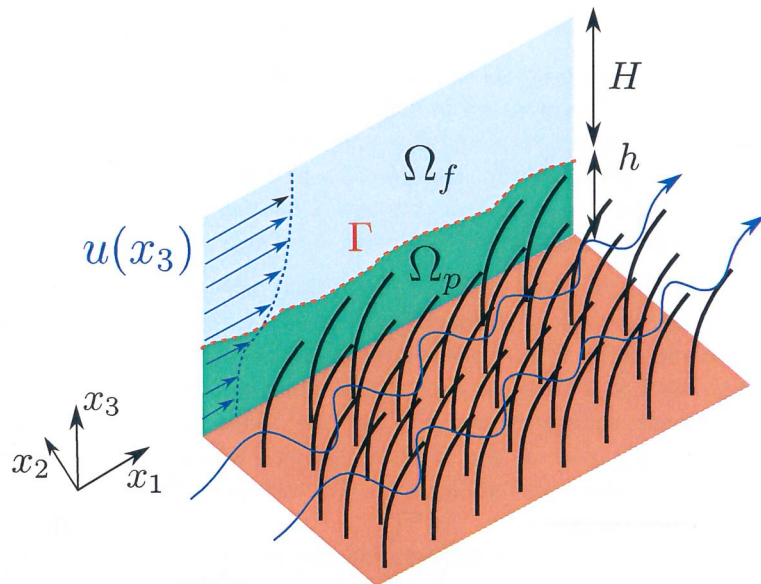


Figure 1.13: Sketch of a fully developed flow over a poroelastic surface made of multiple filaments.

to resolve this complex dynamic one should use a very fine numerical mesh (highly computational expensive) or come up with a model (like in the context of turbulence modeling). Turbulence dynamic can be also problematic; the hypothesis that pore size eddies can exist deep inside the porous medium is still ~~accepted~~ in the community. How to deal with such small scale dynamic and/or find a model is not an easy task.

- Compliance (fluid-structure interaction): if the filaments are flexible, they can bend and swing due to the fluid load. We have to take into account a structural model for the filaments (for example Bernoulli beam), including also the computation of energy that the swing motion re-inject inside the fluid. This two-way coupling could also be really computational expensive in presence of a large number of filaments. If the flexibility is important, one should in principle take into account also the contact and repulsion (elastic coupling) between the fibers. If the porous medium has more complicated shapes (like the scales in the butterfly wing) to come out with a simplified model for the solid dynamic is even harder and the use of a general finite elements discretization is probably a necessity (increasing also the computational cost of the problem). Another approach consists of derive a "rheology" model for the medium, in which the average mechanical properties can be derived. Such models are applicable only to porous media where the solid inclusions are connected to each other. Such average methods are convenient computationally speaking but their mathematical

(by using,
for example,
the Bernoulli
beam equation)

object of some debate

description can be difficult.

to

- Anisotropy: the model used should be capable of treat permeable surfaces that have different responses when stressed in different directions. For instance, the geometrical arrangement disposition and/or the mechanical properties of the medium can be non-homogeneous, so that the medium can appear more permeable in one direction and show a preferential flow path. The different reaction for a specific direction can be modeled with a tensorial parameter as for the case of the permeability tensor that is basically a generalized drag coefficient.

TRATTINO

Dupont et al. [44] performed a LES simulation introducing a two-way coupling for the fluid-structure interaction problem over a carpet of fibers. They validate their simulation with video recording of a similar experiment and the frequency measurements of the Kelvin-Helmholtz instabilities at the interface agrees very well. They have not specified the computational configuration used, but they have mentioned an important high performance computing center in the acknowledgment which made us assume that the computational power involved was substantial. Recently, also Marjoribanks et al. [93] have adopted a similar approach has been used.

Some other examples that solve the full coupled problem directly are Pinelli et al. [116], Favier et al. [50] and Revell et al. [126], but in these cases the number of filaments is small and so they can be though more as isolated filaments rather than a poroelastic carpet medium.

assimilated to

discussed by

their cases

Due to the computationally cost of solving the problem directly, the scientific community has came out with other approaches that treat the porous domain with a generalized model that does not resolve the fine scale inside the filaments, but instead express them as a function of the length scales present in the fluid domain Ω_f .

These are called homogenization approaches and the key point in such methods are:

- The division of the overall domain in two different parts: the fluid domain Ω_f and the porous domain Ω_p .
- Two different fluid models are used in the two domains. In Ω_f the Naver-Stokes equations for incompressible Newtonian fluids are solved. In the porous part there are a number of different models that adds source terms in the former equations to take into account the presence of the porous medium;
- The two domains should be coupled together with a boundary condition at the interface or a transitional region around the interface is added with its specific treatment;
- A model for the structural mechanics. It can be an averaged model or it can solve the mechanics equations directly.

discussed

The key points shown above are extensively explained, in chapter 2, for the homogenization method chosen in this thesis. However, in the next section the two main branches in literature, that take into account the presence of a porous medium layer, are summarized in order to give a panoramic on the possible choices.

1.4.1 Isotropic drag models

In the case of flow through vegetation (canopy flows) it is common to use an isotropic drag model¹ to parameterize the drag of the canopy. The drag can be a function of the wall normal direction, but in most of the applications it is taken as a constant. The isotropic hypothesis can be correct in case of dense vegetation, even if the normal component of the resistance should be smaller. However the resistance in the vertical direction can be approximated in this manner in channel flows where the mean flow is mostly streamwise. On the contrary, in applications where the transpiration at the interface is important (wake control of bluff body) the isotropic drag model is, certainly, not the most adequate.

The drag resistance is included in the Navier-Stokes equations as a source term:

$$\frac{\partial \mathbf{v}_\beta}{\partial t} + \mathbf{v}_\beta \cdot \nabla \mathbf{v}_\beta = -\frac{1}{\rho_\beta} \nabla p_\beta + \nu_\beta \nabla^2 \mathbf{v}_\beta - \frac{1}{2} C_D a |\mathbf{v}_\beta| \mathbf{v}_\beta, \quad (1.4)$$

Where the subscript β indicate variables defined in the fluid phase, and C_D the drag coefficient of the isolated fiber. The parameter a is the frontal area per unit volume of the vegetation, and it is function of the porosity of the medium. The drag term is quadratic in the velocity, but there is some evidence in literature that the reconfiguration phenomena can change this relationship (Gosselin and De Langre [66], and Alvarado et al. [4]).

From our point of view this approach lacks of strong mathematical formalism. As a matter of fact the definition of the additional terms of the equations heavily relies on empirical relations. Another issue is that the isotropic hypothesis rules out the possibility to model the anisotropic nature of most surfaces in which we are interested².

In the field of flows through vegetation some authors have successfully used this approach, for example Maza et al. [96] and Maza et al. [97] used it to study wave attenuation and Ghisalberti and Nepf [58], Battiato and Rubol [11] developed simple models for the 2D mean flow over a canopy.

1.4.2 Homogenization models

In this section we want to introduce the most used approach to derive the equations valid in the porous domain. The fundamental idea is to build a micro-scale model, either for the fluid and for the solid, and then derive the macro-scale equations using some averaging operator over the micro-scale.

The two most used homogenization methods are the *Volume Averaging* method (Whitaker [150]) and the *Multiple Scales* method (Mei and Vernescu [100]) they can be more broadly classified as perturbations methods. The key differences and the main results retrieved using these approaches are presented in the following.

¹the drag is equal in the three principal directions of the medium.

²as equation (1.3) suggest the difference in the permeability along each direction can be important for drag reduction.

Volume averaging approach

The method of Volume Averaging has been developed to treat transport equations in porous media applications; in this case the presence of two different length scales is obvious, as it can be evinced by figure 1.14.

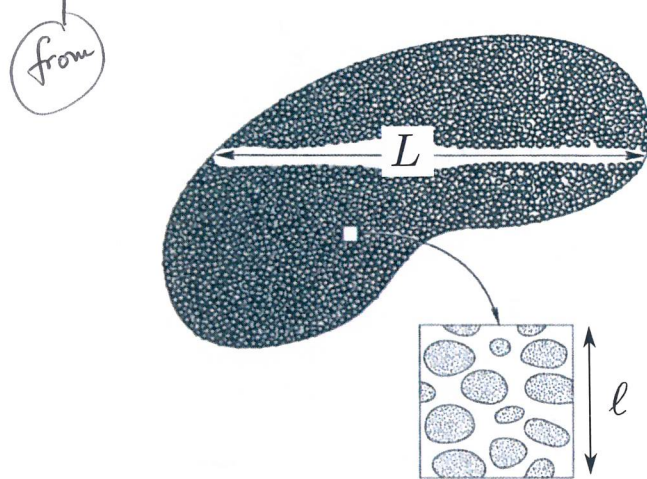


Figure 1.14: Schematics of a porous medium system of size L , with a zoom on the microscopic structure and its scale ℓ . Image from Whitaker [150].

DEFINIE
V
AND
 V_β

The core idea of the methods is to firstly define an average operator as

$$\langle \psi \rangle^\beta = \frac{1}{V_\beta} \int_V \psi dV$$

The equation ψ is

in this case the variable ψ represents any vector or scalar variable in the system of equations that we want to homogenize; for Navier-Stokes they are the velocity and the pressure.

The average operator has the purpose to homogenize the equations, in fact the second crucial step of the method is to decompose the variables as proposed by Gray [67]:

$$\psi = \underbrace{\langle \psi \rangle^\beta}_{O(L)} + \underbrace{\tilde{\psi}}_{O(\ell)}$$

(1.5)

Noindent The equation (1.5) shows how each variable can be decomposed in an averaged part which contains only spatial variations at the macro-scale L and a fluctuation part that contains only the micro-scale ℓ spatial variations.

Also the decomposition can be substituted in the transport equations that we want to average, and after some mathematical manipulations it is possible to retrieve the new

averaged equations that include only variables of order L . Since this is the method chosen to develop our work, all the technical details are explained in chapter 2.

To introduce briefly some other aspects about this method, we show as example, how to derive the homogenized version of the Stokes equation. The described problem is a steady flow inside a rigid porous medium, like the one in figure 1.14. The Stokes equation valid for the fluid phase, indicated with the β subscript, reads:

$$0 = -\nabla p_\beta + \mu_\beta \nabla^2 \mathbf{v}_\beta, \quad (1.6)$$

It is important to specify that equation (1.6) is valid only in the fluid phase and in order to solve it we have to consider a no-slip boundary condition at the interface with the solid phase, with the difficulties that come to define the complex structure of the solid inclusion. Applying the Averaging Method, we can derive a homogeneous version of (1.6) that is valid in all the porous domain that includes the two different phases, the solid and the liquid one. The homogenized version of (1.6) is the well known Darcy equation:

$$\langle \mathbf{v}_\beta \rangle^\beta = -\frac{\mathbf{K}}{\varepsilon \mu_\beta} \nabla \langle p_\beta \rangle^\beta, \quad \text{Darcy's}$$

developed with this approach by Whitaker [147].

The Darcy equation allows to recognize two additional quantities that arise from the averaging procedure, the first one is a scalar called porosity ε that represents the ratio between the volume of the fluid inside a reference volume over the total volume itself. The second one is the tensor \mathbf{K} called permeability tensor and it expresses the resistance of the porous medium that affects the flow in its motion. The term \mathbf{K} plays the same role as C_{Da} in the isotropic drag model; the main difference is that the permeability tensor can be computed directly from the geometry of the medium (see chapter 2), i.e. it does not rely on empirical relations. In addition, the tensorial nature of this terms allows us to model porous inclusions that are anisotropic.

Applications of the theory include flow where inertial terms are not negligible (Whitaker [149]), porous media with small deformations (Whitaker [148]) and with high deformations (Hussong et al. [73]), turbulent problems (Soulaine and Quintard [136], Breugem et al. [23]), interface between a permeable medium and a free flow (Beavers and Joseph [14]), multi-phase systems (Whitaker [145]), heat transfer (Carbonell and Whitaker [32]) and sound propagation (Firdauss et al. [52], Lafarge et al. [86]).

It is impossible to go into detail of the derivation of the equations for each specific problem, but the key point was to show the differences between this method and the isotropic drag model of the previous section.

Multiple Scales

The multiple scales method presents analogies to the previous one and it has also been applied to similar problems in the context of porous media applications.

In this method we start with the assumption of scale separation between ℓ , the micro-scale, and L , the macro-scale. The scale separation factor can be defined as $\epsilon = \ell/L \ll 1$. Using the same examples as the previous section, we show how to compute the homogenized version of the Stokes equation for fluid flow through porous media. We introduce the micro-scale and the macro-scale coordinates defined respectively as:

$$X_i = \frac{\tilde{x}_i}{L}, \quad x_i = \frac{\tilde{x}_i}{\ell},$$

where x_i are the original eulerian coordinate of the problem. Using the above separation factor it is possible to expand the pressure and velocity as:

$$\psi(X_i, x_i) = \psi^{(0)}(X_i, x_i) + \epsilon\psi^{(1)}(X_i, x_i) + \epsilon^2\psi^{(2)}(X_i, x_i) + O(\epsilon^3),$$

Substituting this decomposition inside the equation (1.6) it is possible to derive a set of hierarchical equations, one for each order of the expansion. It can be shown that analyzing each equation in the set the homogenized equation yields:

$$v_i^{(0)} = -K_{ij} \frac{\partial p^{(0)}}{\partial X_j}, \quad (1.7)$$

In which either the pressure or the velocity fields appears only at the order zero, and the equation depends only on the macro-scale length.

Simple The same permeability tensor \mathbf{K} as before is found, with the same definition and interpretation. It is clear that for this ~~problem~~ problem we end up with the same ~~equation~~ homogenized equation; the point that has changed is the starting hypotheses of the method and the mathematical development ~~to compute them~~.

A full analysis of the dualism of the two approaches can be found in the work by Davit et al. [41].

The multiple scales method has also been used to study many other problems: inertial effects (Mei and Auriault [99], Skjetne and Auriault [134]), coupling between a free fluid and a porous media (Mikelic and Jäger [101]), porous media with small deformations (Auriault and Sanchez-Palencia [7]), heat conduction in composites (Auriault [8]), rigid and moving permeable layers (Zampogna and Bottaro [155], Lācis et al. [85] and Zampogna and Bottaro [157]).

1.5 Stability of flows over permeable surfaces

Flows through submerged aquatic plants exhibit large scale vortices at the top of the vegetation, advected along the flow direction and causing a periodic waving of the plants, referred to as monami (if the fluid is air) and honami (in case of water) Inoue [75], Ackerman and Okubo [1]. The effect of the onset of the monami is depicted in figure 1.17.

qualitatively

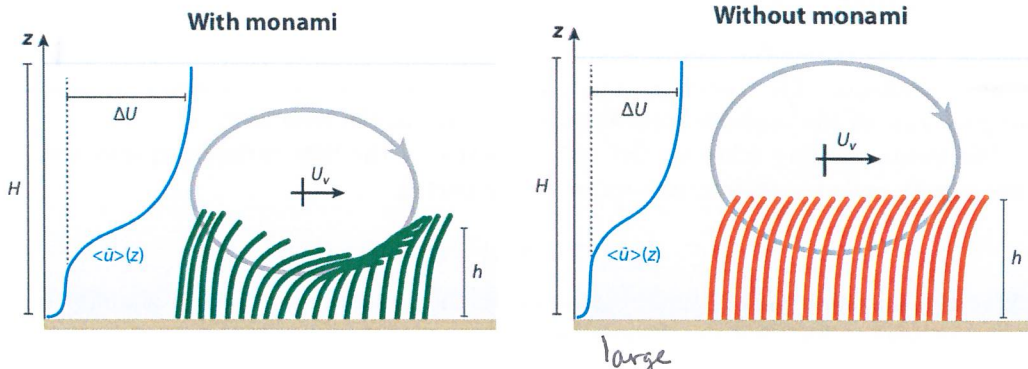


Figure 1.15: Left: when the drag of the canopy is ~~high~~ enough it generates canopy-scale vortices by Kelvin-Helmholtz instability. These vortices may interact with the flexible vegetation and generate a waving motion called monami. Right: when this interaction is too weak, the canopy only bend. Image from Nepf [106].

Vortices arise from the nonlinear amplification of a Kelvin-Helmholtz instability mode, related to the presence of an inflection point in the base flow profile (Asaeda et al. [6]); the profile itself is inflectional because the fluid is slowed down by the drag exerted by the canopy, whose modeling has recently been addressed (Py et al. [117]; Singh et al. [133]; Zampogna et al. [159]; Tilton and Cortelezzi [139]). The correct prediction of the onset and characteristics of the Kelvin-Helmholtz instability ~~are~~ is important to assessing the effects of turbulence (Finnigan [51], Jimenez et al. [79]) in particular to:

- understand how the vertical exchange of momentum occurs (Ikeda and Kanazawa [74]).
- clarify how the transport of CO₂ and dissolved nutrients or sediments take place. This exchange occur between the obstructed vegetation flow and the free overflow motion (Gambi et al. [55], Eckman [45], Grizzle et al. [69]).
- ~~assess~~ the changes in the morphology of the vegetation in inland or coastal wetlands in response to continuous periodic forcing (Asaeda et al. [6], Patil and Singh [113]).

One of the possible approaches to study how and when these instabilities start is the linear stability analysis. In the following section we briefly introduce the key assumption and simplifications of the method, and in the next section some results in the context of permeable surfaces are presented.

1.5.1 Stability theory generalities

Stability theory covers the modeling of transition of fluid systems towards unstable states eventually leading to such as turbulence. The theory gives us a fast and robust method to compute the frequency and grow rate of the unstable modes, if there is any, in the base flow.

The linear stability relies on the decomposition of the flow variables \mathbf{q} into a steady-state part $\bar{\mathbf{q}}$, called base flow, and an unsteady part $\tilde{\mathbf{q}}$:

$$\mathbf{q}(\mathbf{x}, t) = \bar{\mathbf{q}}(\mathbf{x}) + \tilde{\mathbf{q}}(\mathbf{x}, t)$$

Where the unsteady part is small compared to the steady one. We also simplify $\tilde{\mathbf{q}}$ with the hypothesis to have a general wave form:

$$\tilde{\mathbf{q}} = \hat{\mathbf{q}}(\mathbf{x}) e^{i\Theta(\mathbf{x}, t)}$$

where $\hat{\mathbf{q}}$ is the amplitude function and Θ is the phase of the perturbation. The choice made to determine the time and space dependence of either the phase function and the amplitude determine a certain hierarchy inside the stability theories. This hierarchy depend on how many directions we consider to be periodic in the amplitude function³. Figure 1.16 below present each possible choice in literature and the theory that derives from it.

	Denomination	Basic state assumption	Amplitude function	Phase function Θ
Global	TriGlobal PSE-3D	$\partial_1 \bar{\mathbf{q}} \ll \partial_2 \bar{\mathbf{q}}, \partial_3 \bar{\mathbf{q}}$	$\bar{\mathbf{q}}(x_1, x_2, x_3)$ $\bar{\mathbf{q}}(x_1^*, x_2, x_3)$	$\hat{\mathbf{q}}(x_1, x_2, x_3)$ $\hat{\mathbf{q}}(x_1^*, x_2, x_3)$
	BiGlobal	$\partial_1 \bar{\mathbf{q}} = 0$	$\bar{\mathbf{q}}(x_2, x_3)$	$\hat{\mathbf{q}}(x_2, x_3)$
Nonlocal	PSE	$\partial_1 \bar{\mathbf{q}} \ll \partial_2 \bar{\mathbf{q}}, \partial_3 \bar{\mathbf{q}} = 0$	$\bar{\mathbf{q}}(x_1^*, x_2)$	$\hat{\mathbf{q}}(x_1^*, x_2)$
Local	OSE	$\partial_1 \bar{\mathbf{q}} = \partial_3 \bar{\mathbf{q}} = 0$	$\bar{\mathbf{q}}(x_2)$	$\hat{\mathbf{q}}(x_2)$

Figure 1.16: Classification of modal linear stability theories. Table ~~copied~~ from Juniper et al. [80].

In our case we have limited our study to a local approach build on mode decomposition, *local stability theory* (LST, also known as *ordinary stability equations* OSE in the denomination of figure 1.16). In the LST we make the hypothesis that the amplitude and the base flow depend only on the wall normal spatial coordinate (parallel flow) and the phase function take into account the periodicity in time and in the streamwise and cross-flow directions. The last hypothesis should not only be seen as a simplification since there are some ~~class~~ of problems (such as canopy flows) in which two of the three directions are really homogeneous. The complete formulation is in the following equation:

$$\tilde{\mathbf{q}}(\mathbf{x}, t) = \hat{\mathbf{q}}(x_2) e^{i(\alpha x_1 + \beta x_3 - \omega t)}$$

³The hierarchy goes from local approach with 2 direction periodic out of 3, to tri-global with all the 3 directions considered space dependent.

where x_2 is the wall normal direction, α is the streamwise (x_1) wavenumber, β is the crossflow (x_3) wavenumber and ω is the temporal frequency.

Casting this form for the pressure and velocity inside the Navier-Stokes equation, the equations that we get describe the evolution of the perturbations, taking the base flow as an input of the problem. In order to study the stability of the perturbations in their time evolution, problem known as *temporal stability*, we fix the space perturbation form imposing α and β as real numbers (inputs of the problem) and solving for ω as a complex number. With such choices the problem became a generalized eigenvalue for ω :

$$A\hat{\mathbf{q}} = \omega B\hat{\mathbf{q}}$$

problem

The solution gives the frequency (real part of the eigenvalues) and the growth-rate (imaginary part) of the perturbation modes (eigenvectors) of the flow.

The above introduction of the method is quite condensed, however there is ~~available~~ much literature on the subject (Juniper et al. [80], Criminale et al. [38], Schmid and Henningson [129]). The problem has also been extensively studied in its computational aspects by Canuto et al. [31].

1.5.2 Monami/Honami and Kelvin-Helmholtz rolls

We have already highlighted that the above framework concerning the stability problem has been applied in some porous media flow (canopy) configurations, also including the vegetation movement. Because of the flexibility of the vegetation, some theoretical studies have focused on the modeling of the stems of the aquatic plants and their displacement in response to the forcing by the water flow (Py et al. [117]; Patil and Singh [113]; Gosselin and De Langre [65]; Py et al. [118]).

It has been studied in Finnigan [51] that these large coherent structures control turbulence dynamics over the canopy. Movements of the latter generate sweeps (and ejections) of fluids that generates the counter-rotating stream-wise eddy evolving as Kelvin-Helmholtz rolls. The complex evolution of vortices is shown in figure 1.17.

However, Kelvin-Helmholtz vortices occur whether the plants bend or not, and to ascertain causes and effects to first order it is acceptable to focus on rigid porous structures. The flow over and through a submerged array of rigid, cylindrical pillars has been the basis of the approach of Ghisalberti and Nepf [61], Ghisalberti and Nepf [58] and Ghisalberti and Nepf [60], who have conducted a series of careful experiments. Their results have often been used by fluid dynamicists to put forth and test theoretical hypotheses to predict the frequency and wavelength of the large scale vortical motion, for a variety of conditions. The configuration studied consists of a regular grid of rigid pillars, orthogonal to the surface, of identical height h . In some of the theoretical models proposed to analyze the stability of this system, the Rayleigh equation is used throughout the water channel, with or without a drag term in correspondence of the canopy [Raupach et al. [125]]; Py et al. [117]; Singh et al. [133]; Zampogna et al. [159]; and Luminari et al. [92] have recently demonstrated that the addition

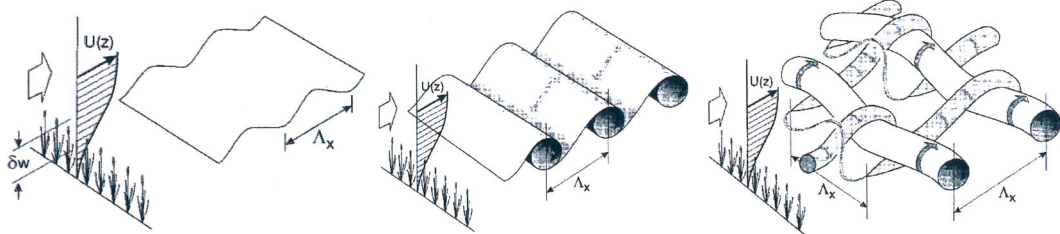


Figure 1.17: Left: first emergence of the Kelvin-Helmholtz instability. The growth-rate is proportional to the shear magnitude at the inflection point. Center: the instability evolves in rollers consisting of high vorticity that are spaced with a similar wave-length Λ_x as the previous stage. Right: secondary instabilities in the rollers lead to their kinking and pairing, coherent structures appear in the transverse and streamwise dimensions. Image from Finnigan [51].

of a drag term through the vegetation reduces the amplification factor of the Kelvin-Helmholtz instability throughout the whole range of wave-numbers and increases mildly the wavelength of the fastest growing mode. In chapter 3 we study how the perturbation of the base flow affects the predicted amplification factor and wavelength. We also test the difference between the isotropic drag model and the tensorial approach, in order to show which ~~scheme~~ robust approach for stability computations.

approach is more

1.6 Conclusions

The key points of this introductory chapter were to first present the context of this research. We have started explaining that the idea of porous surface as aerodynamical performance enhancement came from various examples in Nature. Many models based on this idea already exist and we gave an extensive summary of the results present in literature. We have also presented the key points of the mathematical methods used to derive the porous medium equation that supply a basis for the next chapter in which the volume average method is formally explained. Some of the results and the context of the chapter 3 has been also presented to clarify the connection between the stability analysis and the porous flows.

uping

the

stems

HM VERAMENTE
"CHARITO IL COLLEGAMENTO" ?

Chapter 2

Volume Average Method

Do not worry about your difficulties in mathematics; I can assure you that mine are still greater.

- Letter to junior high school student Barbara Wilson,
January 7, 1943, *Albert Einstein*

2.1 Introduction

In the previous chapter we have already introduced the volume averaging method and how it can be used to derive a macroscopic description of the ~~microscopic~~ system ~~equations~~. The homogenized version of the system is valid everywhere in the porous medium domain, and not only in the fluid phase. Theoretical aspects of the volume averaging method can be found in Whitaker [152], Whitaker [149], Whitaker [151], Quintard and Whitaker [121], Quintard and Whitaker [122], Quintard and Whitaker [123], Quintard and Whitaker [124], Quintard and Whitaker [125] and many others contributions that are introduced in the next chapter. The various steps necessary to derive the local average version of the fluid dynamic equations are listed in the following.

physical

succinctly described

Whitaker [149],
151, 152]
Q & W [.., ..]

2.2 Homogenization procedure

The mathematical method of volume averaging is based on some fundamental steps that one should follow in order to retrieve the homogenized version of the equations. The main steps are:

- Definition of the averaging operator $\hat{\cdot}$
- Use of theorems that permit to interchange the derivation and the averaging operation $\hat{\cdot}$

- Decomposition of fields as a sum of mean field and a perturbed field
- Assumption of length-scales constraints (based on the problem definition) that help to simplify and define a local closure problem

Such schema is graphically resumed in Paéz-Garcia et al. [114] and Davit et al. [41]. A similar flowchart of the complete overall procedure is showed in figure 2.1.

2.3 Derivation of VANS equations for 3D incompressible fluids

2.3.1 Navier-Stokes equations

The dynamic of the fluid phase (indicated with the subscript β), inside and above the porous medium, is governed by the Navier-Stokes equation for incompressible Newtonian fluid:

$$\begin{cases} \frac{\partial \mathbf{v}_\beta}{\partial t} + \nabla \cdot (\mathbf{v}_\beta \mathbf{v}_\beta) = -\frac{1}{\rho_\beta} \nabla p_\beta + \nu_\beta \nabla^2 \mathbf{v}_\beta \\ \nabla \cdot \mathbf{v}_\beta = 0 \\ \mathbf{v}_\beta = \mathbf{v}_\sigma \quad \text{at } A_{\beta\sigma} \end{cases} \quad (2.1)$$

noindent where \mathbf{v}_β , p_β , ρ_β and ν_β stand, respectively, for the velocity, the pressure, the density and the kinematic viscosity of the fluid. The interface between the fluid and the solid is indicated as $A_{\beta\sigma}$, in which the no-slip condition for the velocity apply. In the above boundary condition \mathbf{v}_σ is the velocity of the solid phase. Initial condition should also be specified in order to solve the system, but they do not take active part in the homogenization procedure. The next sections shows how to average this system using the volume averaging method.

2.3.2 Definition of the averaging operators

Figure 2.2 show the schematics of the internal structure of a fibrous porous medium, the important quantities are also indicated in the same picture. The shape of the volumes used in the averaging operations are enclosed in continuous lines. $V|_x$ indicate the volume with centroid x and $V_\beta|_x$ indicate the fluid volume fraction inside the latter. The coordinate $r = x + y$ represent the centroid of another possible volume in which one can compute the average quantities, the boundaries of the same volume are indicated with dotted lines.

Let ψ_β be an arbitrary order tensors (scalar, vector or second order tensor) defined in the fluid phase of the volume V with x as centroid.

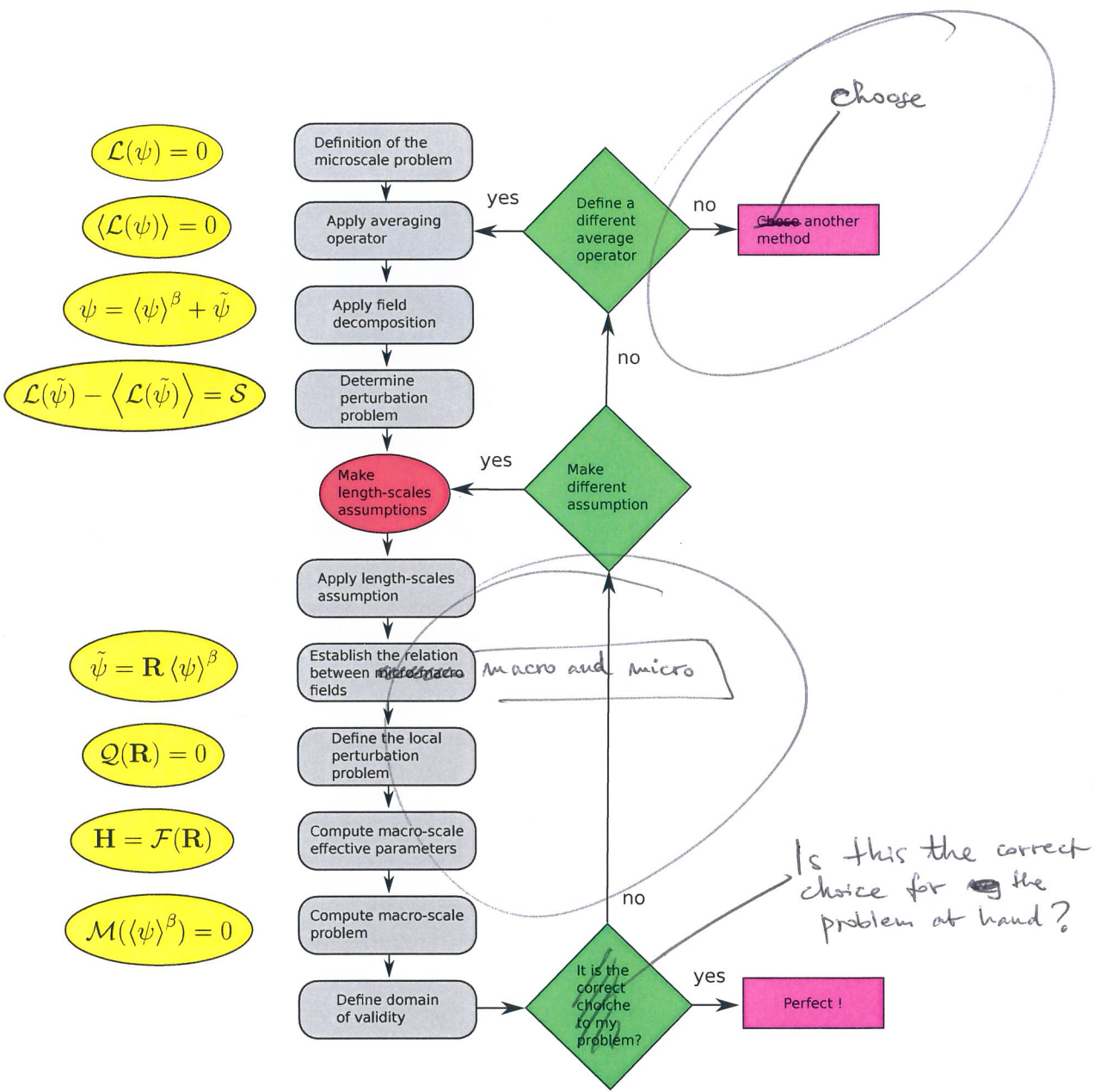


Figure 2.1: Illustration of the volume average homogenization procedure. Image adapted from Davit et al. [41]

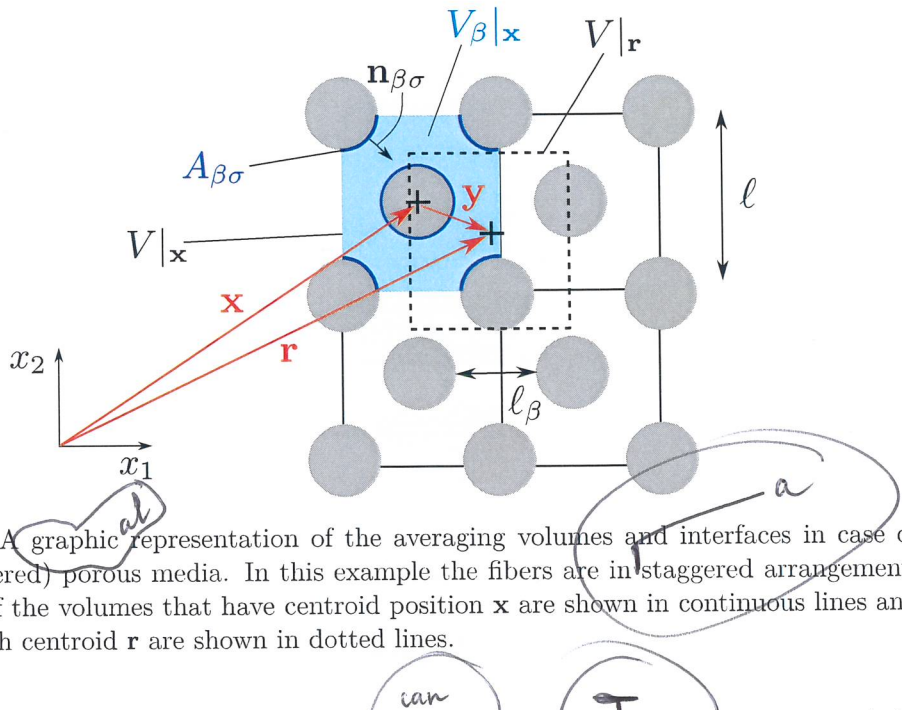


Figure 2.2: A graphic representation of the averaging volumes and interfaces in case of fibrous (ordered) porous media. In this example the fibers are in staggered arrangement. The edges of the volumes that have centroid position \mathbf{x} are shown in continuous lines and the ones with centroid \mathbf{r} are shown in dotted lines.

Two different volume averaging operators should be defined, the *intrinsic average* indicated as $\langle \cdot \rangle^\beta$ reads:

$$\langle \psi_\beta \rangle^\beta |_{\mathbf{x}} = \frac{1}{V_\beta(\mathbf{x})} \int_{V_\beta(\mathbf{x})} m(\mathbf{y}) \psi_\beta(\mathbf{x} + \mathbf{y}, t) dV_\beta, \quad (2.2)$$

where m is a weight function defined on V_β and \mathbf{y} is the relative position vector with respect to the centroid \mathbf{x} of the averaging volume V_β .

The second one is the *superficial average* indicated with $\langle \cdot \rangle$:

$$\langle \psi_\beta \rangle |_{\mathbf{x}} = \frac{1}{V} \int_{V_\beta(\mathbf{x})} m(\mathbf{y}) \psi_\beta(\mathbf{x} + \mathbf{y}, t) dV_\beta, \quad (2.3)$$

In the two definitions \mathbf{y} is the integration variable. The difference between the two formulations is that the former takes into account the actual fluid fraction in averaging the ~~field~~ ~~size~~ instead of the ~~pure~~ size of the total volume.

In order to use a less heavy notation, the subscript $|_{\mathbf{x}}$ is dropped in the following procedure, but should be kept in mind that the volume averaged quantities are explicitly dependents on the center position of the volume as both averaging operators are defined as a volume integral. The size and shape of the integration domain can also be problematic and more details on this issues are presented in the paragraph 2.3.3.

In the definition of the average operators it is possible to introduce a weight function m which has the aim to guarantee smooth volume averaged fields. However, the choice of m depends on the porous media geometry, as the size of the average volume.

The notation is further simplified if a constant weight is considered ($m = 1/V$), in such case it is possible to drop it from the average operators. However any shape of the function m can be used without formally changing the final form of the averaged equations.

The porosity of a porous medium cell is defined as:

$$\varepsilon = \frac{V_\beta}{V} \quad (2.4)$$

which represents how much fluid is actually present inside the averaging volume, in other terms it is an indication of how packed are the fibers of our porous medium.

Using the above definition, it is possible to express a relationship between the two averaging operators:

$$\langle \psi_\beta \rangle = \varepsilon \langle \psi_\beta \rangle \quad (2.5)$$

2.3.3 Choice of shape and size of averaging volume and weight function

The problem of choosing the right weight function, for a given geometry of the porous medium, has been extensively studied by the series of works Quintard and Whitaker [121] - [125], Quintard and Whitaker [122], Quintard and Whitaker [123], Quintard and Whitaker [124], Quintard and Whitaker [125] and more recently generalized by Davit and Quintard [40].

The authors above differentiate their results for ordered and disordered porous media. They show that in each case a specific size and shape of the weight function (and the volume) is needed. The volume in which the average procedure is applied is called *reference elementary volume* (REV). Usually for disordered porous media a spherical volume is the most appropriate, and the REV size (ℓ) should satisfy the length scale constraint:

PERCETE ? ?? $\ell_\beta \ll \ell$??

$\ell_\beta \ll \ell \ll L$

where ℓ_β is a characteristic distance of the pore spacing. Instead in case of ordered porous media the most appropriate shape is usually a cube with side:

$$O(\ell_\beta) = \ell \ll L$$

The above constraint can be reinterpreted as the separation of scale parameter in the multiple scale method, $\epsilon = \ell/L \ll 1$.

Ochoa-Tapia and Whitaker [110] confirm the same length-scale constraints even in case of an interface between a free fluid and a porous medium.

The size of the REV (ℓ) should be chosen with the above specifications. These length scale constraints ensure that the volume is large enough that periodic boundary conditions can be applied in the exterior of the volume. Anyhow the REV size should also capture all

shown

the phenomena that take place at the micro-scale (ℓ_β). If the REV size is the correct one, increasing or decreasing its size should not change the average quantities. The weight function can also help to attenuate variation of the averaged fields due to geometrical inhomogeneities of the porous medium. As a matter of fact, it acts as a low-pass filter for the perturbations fields.

The weight function can also play an important role in the interpretation of the averaged equation. As shown later on, in order to retrieve a local form of the VANS equations, the following statement should in principle be true:

$$\langle \langle \psi_\beta \rangle \rangle|_x = \langle \psi_\beta \rangle|_x \quad (2.6)$$

This means that the averaged field contain small variations at the micro-scale (inside the averaging volume V). In order to satisfy this requirement certain weight functions can perform better than others, although the same conclusion can be derived from the length-scales constraints. In paragraph 2.7, at the end of this chapter, some details of this approximation are further explained.

For disordered porous medium the *hat function* m^\square which has the form:

$$m^\square(y) \begin{cases} \frac{1}{V} & |y| \leq r_0 \\ 0 & |y| > r_0 \end{cases} \quad \text{COSA } \epsilon - r_0 ?? \quad (2.7)$$

can be used to produce smooth averaged fields.

Instead for ordered porous medium the literature shows that triangle shaped function called *cellular filter*, m^Δ , performs better:

$$m^\Delta(y) \begin{cases} (\ell/2 - |y|) & |y| \leq r_0 \\ 0 & |y| > r_0 \end{cases} \quad (2.8)$$

Davit and Quintard [40] have recently expanded the required hypothesis that a m function should satisfy. In general the weight function m should:

- be normalized as: $\int_{V_\beta} m(y) dV_\beta = 1$
- have compact support
- satisfy: $m * \psi_\beta \in C^k$, where k represent the order of the closure
- satisfy: $(m \mathcal{P}^j(y)) * \psi_\beta \begin{cases} 0 & \text{if } j \text{ odd} \\ \text{const} & \text{if } j \text{ even} \end{cases}$

$$=?$$

44

Poco chiaro

SPIEGA



W_{incident} Where $\mathcal{P}^j(\mathbf{y})$ is a polynomial of order j . The last requirement uses the fact that the average operation can also be defined as a convolution product between the weight function and the flow field quantities (Marle [96]):

$$\langle \psi_\beta \rangle|_{\mathbf{x}} = \frac{1}{V} \int_{V_\beta(\mathbf{x})} m(\mathbf{y}) \psi_\beta(\mathbf{x} + \mathbf{y}, t) dV_\beta = m * \psi_\beta$$

The choice of the weight function shape is very important, however previous works in which the authors had implicitly used m^\top are not wrong. As a matter of fact, if the assumption of well behaved fields holds¹ then the homogenized equations are the correct one. However neglecting the use of the proper weight function can induce some problem on the interpretations of the averaged fields²; as a consequence particular care should be used especially when making comparison to experiments.

In the following derivation of the equation no weight function is used inside the averaged operators, in order to not make the notation heavy. In any case in the following text is indicated whether this special hypothesis on the weight function is needed. ? text??

2.3.4 Theorems involving derivatives of spatial averaged quantities

The purpose of these theorems is to be able to swap the derivative and the volume average operation.

Theorem 1 (Spatial averaging theorem). *Let ψ_β be a scalar quantity defined in the fluid phase β , then:*

$$\langle \nabla \psi_\beta \rangle = \nabla \langle \psi_\beta \rangle + \frac{1}{V} \int_{A_{\beta\sigma}} \psi_\beta \mathbf{n}_{\sigma\beta} dA \quad (2.9)$$

In the above $\langle \psi_\beta \rangle$ is evaluated at \mathbf{x} and the operator ∇ express the differentiation operation respect to \mathbf{x} . es

Corollary 1 (Vector form of (2.9)). *The vector form of the spatial averaging theorem is given by:*

$$\langle \nabla \cdot \psi_\beta \rangle = \nabla \cdot \langle \psi_\beta \rangle + \frac{1}{V} \int_{A_{\beta\sigma}} \psi_\beta \cdot \mathbf{n}_{\sigma\beta} dA \quad (2.10)$$

Corollary 2. *Applying the theorem (2.9) to a constant field $\psi_\beta = 1$ the following relation can be found:*

$$\nabla \varepsilon = - \int_{A_{\sigma\beta}} \mathbf{n}_{\sigma\beta} dA, \quad (2.11)$$

¹it means that the equation (2.6) can be verified a posteriori.

²as Quintard and Whitaker [121] show for the example case of hydrostatic pressure.

Reynolds)

Theorem 2 (Reynolds transport theorem). Let ψ_β be a quantity defined in the fluid phase β , then:

$$\frac{\partial}{\partial t} \int_{V_\beta(t)} \psi_\beta dV = \int_{V_\beta(t)} \frac{\partial \psi_\beta}{\partial t} dV + \int_{A_{\beta\sigma}(t)} \psi_\beta (\mathbf{v}_\sigma \cdot \mathbf{n}_{\beta\sigma}) dA, \quad (2.12)$$

— where \mathbf{v}_σ is the point velocity of the solid-fluid interface $A_{\beta\sigma}$.

The three theorems and the corollary are essential to develop the closed form of the equations. One interesting thing to pay attention is that the theorems switch the average and derivative operation but always introduce a non local integral term.

2.3.5 Averaged continuity equations

We start by finding the averaged version of the continuity equation in (2.1):

$$\langle \nabla \cdot \mathbf{v}_\beta \rangle = 0 \quad (2.13)$$

— Applying theorem (2.9) to the previous equation we get:

$$\langle \nabla \cdot \mathbf{v}_\beta \rangle = \nabla \cdot \langle \mathbf{v}_\beta \rangle + \frac{1}{V} \int_{A_{\beta\sigma}} \mathbf{v}_\beta \cdot \mathbf{n}_{\sigma\beta} dA$$

The boundary condition at the interface ($\mathbf{v}_\sigma = \mathbf{v}_\beta$) implies that the integral above can be modified as:

$$= \nabla \cdot \langle \mathbf{v}_\beta \rangle + \frac{1}{V} \int_{A_{\beta\sigma}} \mathbf{v}_\sigma \cdot \mathbf{n}_{\sigma\beta} dA.$$

Now we rewrite the last term as if it were a result of the Reynolds transport theorem applied to a constant unitary scalar field:

$$= \nabla \cdot \langle \mathbf{v}_\beta \rangle + \frac{\partial}{\partial t} \left(\frac{1}{V} \int_{V_\beta} dV \right) - \frac{1}{V} \int_{V_\beta} \frac{\partial}{\partial t} \left(\frac{1}{V} \int_{V_\beta} dV \right),$$

where the last integral is zero due to the time derivation of a constant field. The first term can be further developed, obtaining finally the averaged continuity equation:

$$\nabla \cdot \langle \mathbf{v}_\beta \rangle + \frac{\partial \varepsilon}{\partial t} = 0 \quad (2.14)$$

2.3.6 Averaged momentum equations

We seek the average version of the momentum equation in (2.1) re-written below:

$$\frac{\partial \mathbf{v}_\beta}{\partial t} + \nabla \cdot (\mathbf{v}_\beta \mathbf{v}_\beta) = -\frac{1}{\rho_\beta} \nabla p_\beta + \nu_\beta \nabla^2 \mathbf{v}_\beta \quad (2.15)$$

In order to keep the procedure readable the development of each term is performed separately, in the same order as they appear in equation (2.15).

Temporal derivative term

Using theorem (2.12) we can rewrite the first term of the equation as:

$$\left\langle \frac{\partial \mathbf{v}_\beta}{\partial t} \right\rangle = \frac{\partial \langle \mathbf{v}_\beta \rangle}{\partial t} - \frac{1}{V} \int_{A_{\beta\sigma}} \mathbf{v}_\beta (\mathbf{v}_\sigma \cdot \mathbf{n}_{\sigma\beta}) dA \quad (2.16)$$

Convective term

Theorem (2.10) applied to the convective term gives us:

$$\langle \nabla \cdot (\mathbf{v}_\beta \mathbf{v}_\beta) \rangle = \nabla \cdot \langle \mathbf{v}_\beta \mathbf{v}_\beta \rangle + \frac{1}{V} \int_{A_{\beta\sigma}} (\mathbf{v}_\beta \mathbf{v}_\beta) \cdot \mathbf{n}_{\sigma\beta} dA \quad (2.17)$$

The boundary condition at the interface ($\mathbf{v}_\sigma = \mathbf{v}_\beta$) implies that the integrals inside the convective and temporal part are equal, so the ~~whole~~ left end side of the momentum equation became:

becomes:

$$\text{LHS} = \frac{\partial \langle \mathbf{v}_\beta \rangle}{\partial t} + \nabla \cdot \langle \mathbf{v}_\beta \mathbf{v}_\beta \rangle \quad (2.18)$$

Pressure term

The pressure term is also expanded using theorem (2.9):

$$\left\langle -\frac{1}{\rho_\beta} \nabla p_\beta \right\rangle = -\frac{1}{\rho_\beta} \nabla \langle p_\beta \rangle - \frac{1}{V} \int_{A_{\beta\sigma}} \frac{p_\beta}{\rho_\beta} \mathbf{n}_{\sigma\beta} dA \quad (2.19)$$

Diffusion term

Here we first use the identity $\nabla^2 = \nabla \cdot (\nabla)$, then we apply ~~the~~ theorem (2.10) directly to this expansion to get:

$$\left\langle \nu_\beta \nabla^2 \mathbf{v}_\beta \right\rangle = \langle \nu_\beta \nabla \cdot \nabla \mathbf{v}_\beta \rangle = \nabla \cdot \langle \nu_\beta \nabla \mathbf{v}_\beta \rangle + \frac{1}{V} \int_{A_{\beta\sigma}} \nu_\beta \nabla \mathbf{v}_\beta \cdot \mathbf{n}_{\sigma\beta} dA \quad (2.20)$$

incident ← Now using ~~the~~ theorem (2.9) on $\langle \nabla \mathbf{v}_\beta \rangle$ we get:

$$\begin{aligned} \left\langle \nu_\beta \nabla^2 \mathbf{v}_\beta \right\rangle &= \nabla \cdot \nu_\beta \nabla \langle \mathbf{v}_\beta \rangle + \nabla \cdot \left(\frac{1}{V} \int_{A_{\beta\sigma}} (\mathbf{v}_\beta \mathbf{v}_\beta) \cdot \mathbf{n}_{\sigma\beta} dA \right) + \frac{1}{V} \int_{A_{\beta\sigma}} (\nu_\beta \nabla \mathbf{v}_\beta) \cdot \mathbf{n}_{\sigma\beta} dA \\ &= \nu_\beta \nabla^2 \langle \mathbf{v}_\beta \rangle + \nabla \cdot \left(\frac{1}{V} \int_{A_{\beta\sigma}} (\mathbf{v}_\beta \mathbf{v}_\beta) \cdot \mathbf{n}_{\sigma\beta} dA \right) + \frac{1}{V} \int_{A_{\beta\sigma}} (\nu_\beta \nabla \mathbf{v}_\beta) \cdot \mathbf{n}_{\sigma\beta} dA, \end{aligned}$$

incident

47

Secondo me qui NON
ci va il PUNTO (PRODOTTO SCALARE):

$$\mathbf{v}_\beta \cdot \mathbf{v}_\beta = \{ v_i v_j \}$$

TOGGLI PUNTO (PRODOTTO SCALARE)
E HAI IL GRADIENTE
DI $\nu_\beta \nabla v_\beta$

and using Gauss theorem on the second term we get:

$$\langle \nu_\beta \nabla^2 v_\beta \rangle = \nu_\beta \nabla^2 \langle v_\beta \rangle + \nabla \cdot \left(\frac{1}{V} \int_{V_\beta} \nabla \cdot (\nu_\beta v_\beta) dV \right) + \frac{1}{V} \int_{A_{\beta\sigma}} (\nu_\beta \nabla v_\beta) \cdot n_{\sigma\beta} dA,$$

CONTINUITÀ??

NON
CHÉDO. SEI
SICURO DELLA TUA DERIVAZIONE ??

the second term is zero due to the continuity equation, so the viscous term yields:

$$\langle \nu_\beta \nabla^2 v_\beta \rangle = \nu_\beta \nabla^2 \langle v_\beta \rangle + \frac{1}{V} \int_{A_{\beta\sigma}} (\nu_\beta \nabla v_\beta) \cdot n_{\sigma\beta} dA. \quad (2.21)$$

Before continuing the development, by summing all the terms together we get:
incident ←

$$\begin{aligned} \frac{\partial \langle v_\beta \rangle}{\partial t} + \nabla \cdot \langle v_\beta v_\beta \rangle &= -\frac{1}{\rho_\beta} \nabla \langle p_\beta \rangle + \nu_\beta \nabla^2 \langle v_\beta \rangle + \\ &+ \frac{1}{V} \int_{A_{\beta\sigma}} \left(-\frac{p_\beta}{\rho_\beta} \mathbf{I} + \nu_\beta \nabla v_\beta \right) \cdot n_{\sigma\beta} dA. \end{aligned} \quad (2.22)$$

CONTROLLA LA DERIVAZIONE

This is still not the averaged version of the momentum equation, since it has the presence of the non-homogeneous term $\langle v_\beta v_\beta \rangle$ and the integral term still has the local (microscopic) variables inside. In the next section these two terms are treated in order to make them function of the only averaged quantities.

2.3.7 Length scale decomposition

The decomposition proposed by Gray [68] is now used to get the average version of the problem (2.1):

PERCHE' PEDICE ???

$$\psi_\beta(\mathbf{r}, t) = \langle \psi_\beta \rangle^\beta |_{(\mathbf{r}, t)} + \tilde{\psi}_\beta(\mathbf{r}, t), \quad (2.23)$$

— where $\tilde{\psi}_\beta$ is the microscopic scale contribution and $\langle \psi_\beta \rangle^\beta$ the volume average one. The two contributions should be added together to obtain the local field value for the considered quantity ψ_β . This decomposition has been introduced in order to separate the different scales of the spatial variation of the fields, and so separate the low frequencies from the high ones. $\text{of this decomposition}$

If the hypothesis ~~all the this division~~ holds, it is possible to demonstrate that the average value of the perturbation field ~~vanishes~~⁴:

$$\langle \tilde{\psi}_\beta \rangle = \langle \psi_\beta \rangle - \langle \langle \psi_\beta \rangle^\beta \rangle \approx \langle \psi_\beta \rangle - \varepsilon \langle \psi_\beta \rangle^\beta = \langle \psi_\beta \rangle - \langle \psi_\beta \rangle = 0$$

⁴ paragraph 2.7 specifically addresses the hypothesis behind this result.

PUOI FAR VEDERE NELL'ES
DA DVE SCATURISCE
QUESTA UGUALANZA?

Using the above results, the non-~~nonlinear~~^{linear} term in equation (2.22) can be converted to:

$$\langle \mathbf{v}_\beta \mathbf{v}_\beta \rangle = \left\langle \langle \mathbf{v}_\beta \rangle \langle \mathbf{v}_\beta \rangle^\beta \right\rangle + 2 \left\langle \langle \mathbf{v}_\beta \rangle^\beta \tilde{\mathbf{v}}_\beta \right\rangle + \langle \tilde{\mathbf{v}}_\beta \tilde{\mathbf{v}}_\beta \rangle = \varepsilon \langle \mathbf{v}_\beta \rangle^\beta \langle \mathbf{v}_\beta \rangle^\beta + \langle \tilde{\mathbf{v}}_\beta \tilde{\mathbf{v}}_\beta \rangle \quad (2.24)$$

For each integral term of (2.22) the same field decomposition should be applied:

$$\begin{aligned} \frac{1}{V} \int_{A_{\beta\sigma}} - \left(\frac{p_\beta}{\rho_\beta} \mathbf{I} \right) \cdot \mathbf{n}_{\sigma\beta} dA &= \frac{1}{V} \int_{A_{\beta\sigma}} - \frac{1}{\rho_\beta} (\langle p_\beta \rangle^\beta + \tilde{p}_\beta) \mathbf{n}_{\sigma\beta} dA \\ &= + \frac{1}{\rho_\beta} \nabla \varepsilon \langle p_\beta \rangle^\beta - \frac{1}{V} \int_{A_{\beta\sigma}} \frac{\tilde{p}_\beta}{\rho_\beta} \mathbf{n}_{\sigma\beta} dA \end{aligned} \quad (2.25)$$

$$\begin{aligned} \frac{1}{V} \int_{A_{\beta\sigma}} \nu_\beta \nabla \mathbf{v}_\beta \cdot \mathbf{n}_{\sigma\beta} dA &= \frac{1}{V} \int_{A_{\beta\sigma}} \nu_\beta \nabla (\langle \mathbf{v}_\beta \rangle^\beta + \tilde{\mathbf{v}}_\beta) \cdot \mathbf{n}_{\sigma\beta} dA \\ &= -\nu_\beta \nabla \varepsilon \nabla \langle \mathbf{v}_\beta \rangle^\beta + \frac{1}{V} \int_{A_{\beta\sigma}} \nu_\beta \nabla \tilde{\mathbf{v}}_\beta \cdot \mathbf{n}_{\sigma\beta} dA \end{aligned} \quad (2.26)$$

The momentum equation now reads:

$$\begin{aligned} \frac{\partial \langle \mathbf{v}_\beta \rangle}{\partial t} + \nabla \cdot (\varepsilon \langle \mathbf{v}_\beta \rangle^\beta \langle \mathbf{v}_\beta \rangle^\beta) + \nabla \cdot (\langle \tilde{\mathbf{v}}_\beta \tilde{\mathbf{v}}_\beta \rangle) &= -\frac{1}{\rho_\beta} \nabla \langle p_\beta \rangle + \nu_\beta \nabla^2 \langle \mathbf{v}_\beta \rangle + \\ -\nu_\beta \nabla \varepsilon \nabla \langle \mathbf{v}_\beta \rangle^\beta + \frac{1}{\rho_\beta} \nabla \varepsilon \langle p_\beta \rangle^\beta + \frac{1}{V} \int_{A_{\beta\sigma}} \left(-\frac{\tilde{p}_\beta}{\rho_\beta} \mathbf{I} + \nu_\beta \nabla \tilde{\mathbf{v}}_\beta \right) \cdot \mathbf{n}_{\sigma\beta} dA \end{aligned} \quad (2.27)$$

At this step the momentum equation is not closed since ~~all~~^{both} the averaged quantities and ~~the~~ perturbation fields are present. In order to overcome this problem in the next section the intrinsic version of the equations will be ~~computed~~^{derived}.

2.3.8 Intrinsic average form

In order to get the intrinsic average formulation the relation (2.5) is used to express surface averaged quantities in terms of intrinsic ones.

First, the continuity equation becomes:

$$\nabla \cdot (\varepsilon \langle \mathbf{v}_\beta \rangle^\beta) + \frac{\partial \varepsilon}{\partial t} = 0$$

~~incident~~ ← The temporal derivative term of the momentum equation becomes:

$$\frac{\partial \langle \mathbf{v}_\beta \rangle}{\partial t} = \frac{\partial (\varepsilon \langle \mathbf{v}_\beta \rangle^\beta)}{\partial t} = \frac{\partial \varepsilon}{\partial t} \langle \mathbf{v}_\beta \rangle^\beta + \varepsilon \frac{\partial \langle \mathbf{v}_\beta \rangle^\beta}{\partial t}$$

Applying the same relation to the viscous term yields:

$$\nabla^2 \langle \mathbf{v}_\beta \rangle = \nabla^2 (\varepsilon \langle \mathbf{v}_\beta \rangle^\beta) = \varepsilon \nabla^2 \langle \mathbf{v}_\beta \rangle^\beta + \langle \mathbf{v}_\beta \rangle^\beta \nabla^2 \varepsilon + 2 \nabla \varepsilon \nabla \langle \mathbf{v}_\beta \rangle^\beta \quad (2.28)$$

and the pressure term is also transformed into:

$$\nabla \langle p_\beta \rangle = \nabla (\varepsilon \langle p_\beta \rangle^\beta) = \varepsilon \nabla \langle p_\beta \rangle^\beta + \langle p_\beta \rangle^\beta \nabla \varepsilon \quad (2.29)$$

Summing up all the terms, we get:

$$\begin{aligned} & \frac{\partial \varepsilon}{\partial t} \langle \mathbf{v}_\beta \rangle^\beta + \varepsilon \frac{\partial \langle \mathbf{v}_\beta \rangle^\beta}{\partial t} + \nabla \cdot (\varepsilon \langle \mathbf{v}_\beta \rangle^\beta \langle \mathbf{v}_\beta \rangle^\beta) + \nabla \cdot (\langle \tilde{\mathbf{v}}_\beta \tilde{\mathbf{v}}_\beta \rangle) \\ &= -\varepsilon \nabla \left(\frac{\langle p_\beta \rangle^\beta}{\rho_\beta} \right) - \nabla \varepsilon \frac{1}{\rho_\beta} \langle p_\beta \rangle^\beta + \nu_\beta \varepsilon \nabla^2 \langle \mathbf{v}_\beta \rangle^\beta + \nu_\beta \langle \mathbf{v}_\beta \rangle^\beta \nabla^2 \varepsilon + 2 \nu_\beta \nabla \varepsilon \nabla \langle \mathbf{v}_\beta \rangle^\beta \\ &+ \frac{1}{\rho_\beta} \nabla \varepsilon \langle p_\beta \rangle^\beta - \frac{1}{V} \int_{A_{\beta\sigma}} \frac{\tilde{p}_\beta}{\rho_\beta} \mathbf{n}_{\sigma\beta} dA \\ &- \nu_\beta \nabla \varepsilon \nabla \langle \mathbf{v}_\beta \rangle^\beta + \frac{1}{V} \int_{A_{\beta\sigma}} \nu_\beta \nabla \tilde{\mathbf{v}}_\beta \cdot \mathbf{n}_{\sigma\beta} dA \end{aligned} \quad (2.30)$$

After the proper simplification we have the final versions of the Navier-Stokes system of equations (2.1) using intrinsic quantities:

$$\left\{ \begin{array}{l} \frac{\partial \varepsilon}{\partial t} \langle \mathbf{v}_\beta \rangle^\beta + \varepsilon \frac{\partial \langle \mathbf{v}_\beta \rangle^\beta}{\partial t} + \nabla \cdot (\varepsilon \langle \mathbf{v}_\beta \rangle^\beta \langle \mathbf{v}_\beta \rangle^\beta) + \nabla \cdot (\langle \tilde{\mathbf{v}}_\beta \tilde{\mathbf{v}}_\beta \rangle) \\ = -\varepsilon \nabla \left(\frac{\langle p_\beta \rangle^\beta}{\rho_\beta} \right) + \nu_\beta \varepsilon \nabla^2 \langle \mathbf{v}_\beta \rangle^\beta + \nu_\beta \nabla \varepsilon \nabla \langle \mathbf{v}_\beta \rangle^\beta + \nu_\beta \langle \mathbf{v}_\beta \rangle^\beta \nabla^2 \varepsilon \\ + \frac{1}{V} \int_{A_{\beta\sigma}} \left(-\frac{\tilde{p}_\beta}{\rho_\beta} \mathbf{I} + \nu_\beta \nabla \tilde{\mathbf{v}}_\beta \right) \cdot \mathbf{n}_{\sigma\beta} dA \\ \nabla \cdot (\varepsilon \langle \mathbf{v}_\beta \rangle^\beta) + \frac{\partial \varepsilon}{\partial t} = 0 \end{array} \right. \quad (2.31)$$

It is important to ~~underline~~ highlight that the intrinsic momentum equation explicitly depends on the porosity of the medium, because of the terms involving gradients of the porosity field. In applications where the porosity can vary spatially, like the interface of a porous medium, this formulation has the advantage to treat explicitly the interface non-homogeneities ⁵.

The equation (2.31) is also *non-local* since it has volume-average quantities and surface integrals. These terms need some explicit manipulation in order to get a close formulation of the above system. In the next paragraphs a closure formulation of these terms is discussed. Usually these ~~volume~~ terms of the equations are named ~~volume~~ *sub-filter stresses* ζ and *microscopic force* \mathbf{F}^m :

⁵further discussion of the interface treatment is presented in paragraph 2.5

$$\zeta = \nabla \cdot (\langle \tilde{\mathbf{v}}_\beta \tilde{\mathbf{v}}_\beta \rangle),$$

$$\mathbf{F}^m = \frac{1}{V} \int_{A_{\beta\sigma}} \left(-\frac{\tilde{p}_\beta}{\rho_\beta} \mathbf{I} + \nu_\beta \nabla \tilde{\mathbf{v}}_\beta \right) \cdot \mathbf{n}_{\sigma\beta} dA$$

2.4 Closure problems

2.4.1 Microscopic force \mathbf{F}^m

The term \mathbf{F}^m act as a surface filter in the momentum equation. The perturbation fields are filtered out by the integral operation over the fluid-solid interface. However is usually called microscopic force since it physically represents the force per unit mass that the fluid exerts on the solid inclusions.

There is no simple representation for \mathbf{F}^m if we include the terms that contain gradients of the porosity ($\nabla \varepsilon$). ~~Although~~ Since we are interested in developing a **local** closure problem, which will depend on the geometry of each REV, it is possible to neglect these terms. It means that the closure problems are not correct at the interface between a porous medium and a free fluid. However if we use these closure problems at the interface we can still obtain good results, as shown in the last chapter, even if they are not formally correct.

The continuity equation in ~~the~~ system (2.31) becomes $\nabla \cdot \langle \mathbf{v}_\beta \rangle^\beta = 0$ after the assumption of constant porosity. We subtract this last equation from the continuity equation valid for the local velocity velocity (2.1):

$$\nabla \cdot \mathbf{v}_\beta - \nabla \cdot \langle \mathbf{v}_\beta \rangle^\beta = 0$$

From ~~the~~ Gray decomposition (2.23) the perturbation velocity field is written as $\tilde{\mathbf{v}}_\beta = \mathbf{v}_\beta - \langle \mathbf{v}_\beta \rangle^\beta$, using this relation after grouping the divergence we obtain the continuity equation for the perturbations:

$$\nabla \cdot \tilde{\mathbf{v}}_\beta = 0 \quad (2.32)$$

To continue the development, we first divide the momentum equation present in system (2.31) by the permeability ε , and we also apply the assumption of constant porosity:

$$\begin{aligned} \frac{\partial \langle \mathbf{v}_\beta \rangle^\beta}{\partial t} + \nabla \cdot (\langle \mathbf{v}_\beta \rangle^\beta \langle \mathbf{v}_\beta \rangle^\beta) + \nabla \cdot (\langle \tilde{\mathbf{v}}_\beta \tilde{\mathbf{v}}_\beta \rangle) \\ = -\nabla \left(\frac{\langle p_\beta \rangle^\beta}{\rho_\beta} \right) + \nu_\beta \nabla^2 \langle \mathbf{v}_\beta \rangle^\beta + \frac{1}{V_\beta} \int_{A_{\beta\sigma}} \left(-\frac{\tilde{p}_\beta}{\rho_\beta} \mathbf{I} + \nu_\beta \nabla \tilde{\mathbf{v}}_\beta \right) \cdot \mathbf{n}_{\sigma\beta} dA \end{aligned}$$

↳ *voindent*

Subtracting the above momentum equation from the local field one (2.1) it is found:

$$\frac{\partial \tilde{\mathbf{v}}_\beta}{\partial t} + \mathbf{v}_\beta \cdot \nabla \tilde{\mathbf{v}}_\beta + \tilde{\mathbf{v}}_\beta \cdot \nabla \langle \mathbf{v}_\beta \rangle^\beta + \varepsilon^{-1} \nabla \cdot \langle \tilde{\mathbf{v}}_\beta \tilde{\mathbf{v}}_\beta \rangle = -\nabla \left(\frac{\tilde{p}_\beta}{\rho_\beta} \right) + \nu_\beta \nabla^2 \tilde{\mathbf{v}}_\beta - \frac{1}{V_\beta} \int_{A_{\beta\sigma}} \left(-\frac{\tilde{p}_\beta}{\rho_\beta} \mathbf{I} + \nu_\beta \nabla \tilde{\mathbf{v}}_\beta \right) \cdot \mathbf{n}_{\sigma\beta} dA \quad (2.33)$$

Now in order to simplify this last equation the following length-scale estimates can be introduced:

DA DVE
SALTANO
FUORI ? DM
RIFERIMENTI!
SONO SEMPRE
ACCETTABILI?

$$\tilde{\mathbf{v}}_\beta = O(\langle \mathbf{v}_\beta \rangle^\beta), \quad \nabla \tilde{\mathbf{v}}_\beta = O\left(\frac{\langle \mathbf{v}_\beta \rangle^\beta}{\ell}\right), \quad \nabla \langle \mathbf{v}_\beta \rangle^\beta = O\left(\frac{\langle \mathbf{v}_\beta \rangle^\beta}{L}\right), \quad \varepsilon = O(\delta)$$

COSTA E⁵
δ?
DVE E
SALTATA
INTRODOTTA?

The last relation state that the porosity varies at a scale δ . Valdés-Parada et al. [143] and Ochoa-Tapia and Whitaker [110] propose the estimate $\ell \ll \delta$ arguing that δ has the size of the zone in which the porosity varies, in case of an interface between a porous medium and a free fluid. However it is important to state that this assumption does not holds at the interface of all the porous media geometry. For ordered porous media $\varepsilon = O(\ell)$. Whitaker [151] state clearly that there is no easy way to define a local closure problem when the relation $\ell \ll \delta$ does not hold. In order to continue with the development of the equation, the relationship $\ell \ll \delta$ is assumed to be true. Although the derived closure problem will be formally correct only far from regions where the porosity varies.

Analyzing the ~~estimate~~ order of magnitude it is possible to neglect some of the terms in momentum equation (2.33):

$$\mathbf{v}_\beta \cdot \nabla \tilde{\mathbf{v}}_\beta \gg \tilde{\mathbf{v}}_\beta \cdot \nabla \langle \mathbf{v}_\beta \rangle^\beta \Rightarrow O\left(\frac{\langle \mathbf{v}_\beta \rangle^\beta}{\ell}\right) \gg O\left(\frac{\langle \mathbf{v}_\beta \rangle^\beta}{L}\right) \quad (2.34)$$

$$\mathbf{v}_\beta \cdot \nabla \langle \tilde{\mathbf{v}}_\beta \rangle^\beta \gg \varepsilon^{-1} \nabla \cdot (\langle \tilde{\mathbf{v}}_\beta \tilde{\mathbf{v}}_\beta \rangle) \Rightarrow O\left(\frac{(\langle \mathbf{v}_\beta \rangle^\beta)^2}{\ell}\right) \gg O\left(\frac{(\langle \mathbf{v}_\beta \rangle^\beta)^2}{\delta}\right) \quad (2.35)$$

$$\nu_\beta \nabla^2 \tilde{\mathbf{v}}_\beta \gg \frac{\partial \tilde{\mathbf{v}}_\beta}{\partial t} \Rightarrow O\left(\frac{(\langle \mathbf{v}_\beta \rangle^\beta)^2}{\ell}\right) \gg O\left(\frac{(\langle \mathbf{v}_\beta \rangle^\beta)^2}{L}\right) \quad (2.36)$$

In the last assessment it has been assumed that the time scale associated respectively with the micro and macro-scale are $t = \ell/\langle \mathbf{v}_\beta \rangle^\beta$ and $T = L/\langle \mathbf{v}_\beta \rangle^\beta$. These assumptions imply that the perturbation problem is *quasi-stationary*, since physically the perturbation field can be considered steady from the macroscopic point of view (Davit et al. [41] and Zhu et al. [163]). It can also be notice that in the above simplifications we have neglected terms that contains the small parameter ε or its powers. This last results is coherent with the multiple scale theory in which only zero order terms are kept in the local closure problem formulation.

[Mei & Vernescu]

With this order of magnitude analysis the governing equations are simplified as:

$$\begin{cases} \mathbf{v}_\beta \cdot \nabla \tilde{\mathbf{v}}_\beta = -\nabla \left(\frac{\tilde{p}_\beta}{\rho_\beta} \right) + \nu_\beta \nabla^2 \tilde{\mathbf{v}}_\beta - \frac{1}{V_\beta} \int_{A_{\beta\sigma}} \left(-\frac{\tilde{p}_\beta}{\rho_\beta} \mathbf{I} + \nu_\beta \nabla \tilde{\mathbf{v}}_\beta \right) \cdot \mathbf{n}_{\sigma\beta} dA, \\ \nabla \cdot \tilde{\mathbf{v}}_\beta = 0 \\ \tilde{\mathbf{v}}_\beta = -\langle \mathbf{v}_\beta \rangle^\beta \text{ at } A_{\beta\sigma}, \end{cases} \quad (2.37)$$

and these represent ~~it is included~~ the transport equations system for the perturbation fields.

Considering rigid porous media is possible to derive the boundary condition at the interface, substituting ~~the~~ Gray decomposition inside the boundary condition expression (2.1). As a consequence in this section the solid phase is assumed rigid, although in section 2.6 this model is extended to take into account moving porous media. The above system is still defined on all the porous domain and so we would like to find a way to reduce its size and still obtain the same results. ~~Although it is possible to use Green functions to solve the problem in this form (Wood and Valdés-Parada [153]).~~

~~This can be done restricting the solution region to a single REV, enforcing periodic boundary conditions at the exterior of such volume. Such hypothesis is consistent with the assumption of periodic ordered porous media in which the macroscopic field variation inside the REV are negligible⁶. The problem ~~as stated before becomes~~ on the REV thus becomes:~~

$$\begin{cases} \mathbf{v}_\beta \cdot \nabla \tilde{\mathbf{v}}_\beta = -\nabla \left(\frac{\tilde{p}_\beta}{\rho_\beta} \right) + \nu_\beta \nabla^2 \tilde{\mathbf{v}}_\beta - \frac{1}{V_\beta} \int_{A_{\beta\sigma}} \left(-\frac{\tilde{p}_\beta}{\rho_\beta} \mathbf{I} + \nu_\beta \nabla \tilde{\mathbf{v}}_\beta \right) \cdot \mathbf{n}_{\sigma\beta} dA, \\ \nabla \cdot \tilde{\mathbf{v}}_\beta = 0 \\ \tilde{\mathbf{v}}_\beta = -\langle \mathbf{v}_\beta \rangle^\beta \text{ at } A_{\beta\sigma}, \\ \tilde{p}_\beta(\mathbf{x} + \ell_i) = \tilde{p}_\beta(\mathbf{x}), \quad \tilde{\mathbf{v}}_\beta(\mathbf{x} + \ell_i) = \tilde{\mathbf{v}}_\beta(\mathbf{x}), \quad i = 1, 2, 3, \\ \langle \tilde{\mathbf{v}}_\beta \rangle^\beta = 0. \end{cases} \quad (2.38)$$

In this set of equations the ~~last~~ ^{last} ~~imposed~~ condition $\langle \tilde{\mathbf{v}}_\beta \rangle^\beta = 0$ is imposed to ensure a unique solution.

Now the perturbed field have to be express as a function of some averaged values. Let us introduce the closure tensor \mathbf{R} and the closure vector \mathbf{r} as:

$$\tilde{\mathbf{v}}_\beta(\mathbf{x}) = \mathbf{R}(\mathbf{x}) \cdot \langle \mathbf{v}_\beta \rangle^\beta(\mathbf{x}) + \xi(\mathbf{x}) \quad (2.39)$$

$$\tilde{p}_\beta(\mathbf{x}) = \mu_\beta \mathbf{r}(\mathbf{x}) \cdot \langle \mathbf{v}_\beta \rangle^\beta(\mathbf{x}) + \gamma(\mathbf{x}) \quad (2.40)$$

where $\xi(\mathbf{x})$ is a vector and $\gamma(\mathbf{x})$ a scalar. ~~However~~ Whitaker [151] have demonstrated that the first is null and the second constant. It is very important to point that (2.39) and (2.40) are crucial since a linear correlation between the micro and macro-scale fields is

⁶see paragraph 2.7

Vanishes

53

It is

HAI GR' USATO PRECEDENTEMENTE (VEDI FIG. 2.2), INVOLIRE ALLE VOLTE LA VARIABILE INDIPEN. \mathbf{r} (es. equazione (2.23)) E ALLE VOLTE E' \mathbf{x} , t questo confonde le idee ...

implied. However these relations can be function of the space coordinate \mathbf{x} as explored later in chapter 4.

~~Since it is free to define the tensor \mathbf{R} and the vector \mathbf{r} as we wish~~, Whitaker [151] proposed to define ~~the two quantities with~~ via the following problem:

$$\begin{aligned} \mathbf{R} \text{ and } \mathbf{r} & \quad \left\{ \begin{array}{l} \frac{\mathbf{v}_\beta}{\nu_\beta} \cdot \nabla \mathbf{R} = -\nabla \mathbf{r} + \nabla^2 \mathbf{R} - \frac{1}{V_\beta} \int_{A_{\beta\sigma}} (-\mathbf{r}\mathbf{I} + \nabla \mathbf{R}) \cdot \mathbf{n}_{\sigma\beta} dA \\ \nabla \cdot \mathbf{R} = 0 \\ \mathbf{R} = \mathbf{I} \text{ at } A_{\beta\sigma} \\ \mathbf{r}(\mathbf{x} + \ell_i) = \mathbf{r}(\mathbf{x}), \quad \mathbf{R}(\mathbf{x} + \ell_i) = \mathbf{R}(\mathbf{x}), \quad i = 1, 2, 3 \\ \langle \mathbf{R} \rangle^\beta = 0 \end{array} \right. \quad (2.41) \end{aligned}$$

incident ↪ It is difficult to solve this problem computationally because it is an integral-differential equation. In order to simplify the problem, it is decomposed ~~in~~ into two parts, the solution of the first one gives us the *permeability tensor* and the solution of the second one the *Forchheimer tensor*.

The variables \mathbf{R} and \mathbf{r} are further decomposed as:

$$\mathbf{R} = \mathbf{B} + \mathbf{C}, \quad \mathbf{r} = \mathbf{b} + \mathbf{c}$$

incident ↪ In this manner the micro-macro field relationship can be written as:

$$\tilde{\mathbf{v}}_\beta = \mathbf{B} \cdot \langle \mathbf{v}_\beta \rangle^\beta + \mathbf{C} \cdot \langle \mathbf{v}_\beta \rangle^\beta \quad (2.42)$$

$$\tilde{p}_\beta = \mu_\beta \mathbf{b} \cdot \langle \mathbf{v}_\beta \rangle^\beta + \mu_\beta \mathbf{c} \cdot \langle \mathbf{v}_\beta \rangle^\beta \quad (2.43)$$

incident ↪ Where \mathbf{B} is defined ~~as~~ from the problem!

$$\begin{aligned} \mathbf{B} & \quad \left\{ \begin{array}{l} 0 = -\nabla \mathbf{b} + \nabla^2 \mathbf{B} - \frac{1}{V_\beta} \int_{A_{\beta\sigma}} (-\mathbf{b}\mathbf{I} + \nabla \mathbf{B}) \cdot \mathbf{n}_{\sigma\beta} dA \\ \nabla \cdot \mathbf{B} = 0 \\ \mathbf{B} = -\mathbf{I} \text{ at } A_{\beta\sigma} \\ \mathbf{b}(\mathbf{x} + \ell_i) = \mathbf{b}(\mathbf{x}), \quad \mathbf{B}(\mathbf{x} + \ell_i) = \mathbf{B}(\mathbf{x}), \quad i = 1, 2, 3 \\ \langle \mathbf{B} \rangle^\beta = 0 \end{array} \right. \quad (2.44) \end{aligned}$$

incident ↪ and \mathbf{C} ~~as~~ from:

$$\left\{ \begin{array}{l} \frac{\mathbf{v}_\beta}{\nu_\beta} \cdot \nabla \mathbf{B} + \frac{\mathbf{v}_\beta}{\nu_\beta} \cdot \nabla \mathbf{C} = -\nabla \mathbf{c} + \nabla^2 \mathbf{C} - \frac{1}{V_\beta} \int_{A_{\beta\sigma}} (-\mathbf{c}\mathbf{I} + \nabla \mathbf{C}) \cdot \mathbf{n}_{\sigma\beta} dA \\ \nabla \cdot \mathbf{C} = 0 \\ \mathbf{C} = 0 \text{ at } A_{\beta\sigma} \\ \mathbf{c}(\mathbf{x} + \ell_i) = \mathbf{c}(\mathbf{x}), \quad \mathbf{C}(\mathbf{x} + \ell_i) = \mathbf{C}(\mathbf{x}), \quad i = 1, 2, 3 \\ \langle \mathbf{C} \rangle^\beta = 0 \end{array} \right. \quad (2.45)$$

~~CREDEVO
DI SÌ ...~~

The problems definition for \mathbf{R} , \mathbf{B} and \mathbf{C} do not arise from the direct substitution of (2.42) and (2.43) into the system (2.38) they are instead a choice made to simplify the calculations (Whitaker [151]). Substituting the decomposition (2.39) and (2.40) inside the surface filter \mathbf{F}^m we get:

$$\mathbf{F}^m = \nu_\beta \left(\frac{1}{V_\beta} \int_{A_{\beta\sigma}} (-\mathbf{r}\mathbf{I} + \nabla \mathbf{R}) \cdot \mathbf{n}_{\sigma\beta} dA \right) \langle \mathbf{v}_\beta \rangle^\beta$$

Dividing then the closure variable as in (2.42) is possible to define the *permeability tensor* \mathbf{K} :

$$\frac{1}{V_\beta} \int_{A_{\beta\sigma}} (-\mathbf{b}\mathbf{I} + \nabla \mathbf{B}) \cdot \mathbf{n}_{\sigma\beta} dA = -\varepsilon \mathbf{K}^{-1}$$

incident ← and the *Forchheimer tensor* \mathbf{F} :

$$\frac{1}{V_\beta} \int_{A_{\beta\sigma}} (-\mathbf{c}\mathbf{I} + \nabla \mathbf{C}) \cdot \mathbf{n}_{\sigma\beta} dA = -\varepsilon \mathbf{K}^{-1} \cdot \mathbf{F}$$

incident ← Using the definition to make the changing of variables proposed by Barrere et al. [9]:

$$\mathbf{d} = \varepsilon^{-1} \mathbf{b} \cdot \mathbf{K}, \quad \mathbf{D} = \varepsilon^{-1} (\mathbf{B} + \mathbf{I}) \cdot \mathbf{K} \quad (2.46)$$

$$\mathbf{m} = \varepsilon^{-1} \mathbf{n} \cdot \mathbf{H}, \quad \mathbf{M} = \varepsilon^{-1} (\mathbf{N} + \mathbf{I}) \cdot \mathbf{H} \quad (2.47)$$

incident ← The problem (2.44) can be written as:

$$\left\{ \begin{array}{l} 0 = -\nabla \mathbf{d} + \nabla^2 \mathbf{D} + \mathbf{I} \\ \nabla \cdot \mathbf{D} = 0 \\ \mathbf{D} = 0 \text{ at } A_{\beta\sigma} \\ \mathbf{d}(\mathbf{x} + \ell_i) = \mathbf{d}(\mathbf{x}), \quad \mathbf{D}(\mathbf{x} + \ell_i) = \mathbf{D}(\mathbf{x}), \quad i = 1, 2, 3 \\ \langle \mathbf{D} \rangle^\beta = \varepsilon^{-1} \mathbf{K} \end{array} \right. \quad (2.48)$$

from which is possible to compute the permeability tensor, \mathbf{K} .

the solution of which it becomes

incident ← P the problem (2.45) with the change of variables (2.47) becomes:

$$\begin{cases} \frac{\nu_\beta}{\nu_\beta} \nabla M = -\nabla m + \nabla^2 M + I \\ \nabla \cdot M = 0 \\ M = 0 \text{ at } A_{\beta\delta} \\ m(x + \ell_i) = m(x), \quad M(x + \ell_i) = M(x), \quad i = 1, 2, 3 \\ \langle M \rangle^\beta = \varepsilon^{-1} H \end{cases} \quad (2.49)$$

where H is called *effective permeability tensor* and it represents a generalization of the permeability tensor in the inertia regime. The relation between the Forchheimer tensor and the effective permeability is the following:

$$H^{-1} = K^{-1} (I + F)$$

With the help of the above closure problem the final closed formulation for the microscopic force becomes:

$$F^m \approx F^M = -\nu_\beta \varepsilon H^{-1} \cdot \langle v_\beta \rangle^\beta \quad (2.50)$$

in which it is clear the equivalence between the descriptions by means of the perturbation fields and the one that uses only the macroscopic fields, becomes readily apparent.

However it is possible to use simplified regression that permits to bypass the local closure problem computation and get directly the tensors K and F . One of the most famous relations are the Kozeny-Carman equation [84] and the modified Ergun equation [126]. Extended version of this empirical formulation can be found in Zampogna and Bottaro [157] and Yazdchi and Luding [154]. The above relationships are always based on regressions from experiments and they are usually parameterized with the porosity and some geometrical characteristic of the medium. The downside in using these simplified formulas is that the geometries used are mostly of the time very simple such as spheres, or 2D regular arranged cylinders and they are difficult to generalize. Also their range of application is usually restricted to very small Reynolds number. Such restrictions makes the local closure problem the main reliable source to compute the Forchheimer and permeability tensors.

2.4.2 Sub-filter stresses ζ

The model is not yet completed, also the *sub-filter stresses* need to be closed. This term acts as a volume filter for the perturbation velocity, in fact the product of the velocity perturbation appears inside the volume averaging operator:

$$\zeta = \nabla \cdot (\langle \tilde{v}_\beta \tilde{v}_\beta \rangle)$$

The same term has already been neglected in equation (2.35) in the previous paragraph, based on some length-scale argument. Here we want to explain briefly what this term represents and possibly when it can become important.

Breugem et al. [23] and Nepf [109] separates the nature of sub-filter stresses into two different components:

- *mechanical diffusion*: when the fluid is forced to flow inside the pore, it has to pass around the solid structure causing an augmentation of diffusion inside the VANS momentum equations. This mechanism is usually studied by means of the flow path tortuosity for each different particle.
- *turbulent dispersion*: it is caused by the subfilter scales eddies that appear at the pore scale. This turbulent diffusivity can be anisotropic. For example in case of fibrous porous media the vertical penetration and breakdown of eddies is much higher than the horizontal one.

Breugem et al. [23] shows that even if the two different components are equally important they are negligible in the volume averaged field equations.

However, we speculate that this term can becomes important in situations involving elastic porous media where sweep and diffusion of fluid can be observed at the interface. This statement is supported by Finnigan [51] and De Langre [42] that have shown the turbulence spectrum modification in case of canopy flows. Possibly the sub-filter stresses can model this shift of the spectrum to high frequencies.

In order to better study this term, we need many more reliable full DNS inside the porous media at high pore Reynolds number. However such simulations are very expensive and almost nonexistent literature. Experimental measurements inside the porous structure can be another way to study this volume filter, even though such measurements can be very difficult to perform.

2.5 Interface treatment

The problem of the interface condition between a porous medium and a free fluid has been approached by many different authors. Ehrhardt [47] has given a concise but very clear introduction on the problem, even thought the field is rapidly evolving (Minale [105], Angot et al. [5], Lācis and Bagheri [86] and cite new work of Giuseppe). Our work is not focused on the development of a new condition although, in this paragraph, we want to explain our choice for the interface treatment over the many possible ones.

The interface conditions can be classified in two groups: the *one domain approach* (ODA) and the *two domain approach* (TDA). In the TDA the porous domain is splitted into two and a boundary condition at the interface is specified. Historically the necessity of such a treatment was mainly due by the difference of order of the Stokes equations and the Darcy one, that makes them incompatible at the interface. The Brinkmann model adjusts

the order of the porous media equations, however the validity of this correction deep inside the porous medium is questionable. The TDA was followed by Beavers and Joseph [14], Mikelic and Jäger [103], Ochoa-Tapia and Whitaker [110] and Le Bars and Worster [91]. These works have all in common the fact that a certain slip is specified at the interface, for example the Beavers and Joseph [14] condition reads:

$$\langle v_\beta \rangle^\beta(x, \Gamma^+) = \frac{\sqrt{K} \partial \langle v_\beta \rangle^\beta(x, \Gamma^-)}{\alpha \partial y}$$

where Γ^+ and Γ^- represent the wall normal coordinate above and below the interface, K is a measure of the permeability tensor and α is a coefficient based on the porous medium geometry. Other propositions change and extends this formulation but basically still imposes a velocity jump at the interface, as a function of a parameter α needed to fit the experimental data.

On the contrary in the ODA approach the final averaged equation are valid through the whole domain and the quantities that define the presence of the porous media, i.e. the porosity and permeability, vanish in the free fluid region. This method is also known as penalization method. One of the first porous media application can be found in Caltagirone [30]; after that it was used by many other authors, like Bruneau and Mortazavi [26], Bruneau and Mortazavi [27], Bruneau et al. [28], Hussong et al. [74]. We think that the interface boundary condition approach is not superior, neither physically nor mathematically. As a matter of fact either methods require a parameter to close the formulation. The advantage of using the penalization method is that in this case the parameter needed is the spatial distribution of the porosity field that is trivial to compute when the geometry of the medium is known. Although it is still not clear how to vary the permeability in the transition zone. Most of the authors propose a sharp jump from the porous media value and the free fluid one. Neglecting the variation of permeability at the transition zone appears to be acceptable, even though examples of linear variation of this term exists (Caltagirone [30]). Hussong et al. [74] made a direct comparison with a DNS simulation, for the porosity treatment concluding that the variation of the permeability is very important in order to have a good comparison with high fidelity computation.

A direct comparison between the ODA and TDA is presented in Cimolin and Discacciati [37] that concludes that the macroscopic description of the interface provided by the two different methods is similar. They also point that the penalization method has the advantage to be easily implemented in a Navier-Stokes solver and it does not present sensible convergence properties as the TDA do.

Also, there is evidence in literature (Ochoa-Tapia et al. [111]) that ~~exists~~ the transition zone with the size of the pore scale, in which the velocity and pressure have a continuous variation and not a steep one. It has been demonstrated by the same author that the same transition zone is physical and not a result of the averaging procedure.

In the following work we adopt the penalization approach with the porosity variation computed directly from the geometry of our fibrous medium and a steep variation of the

effective permeability at the interface. In chapter 5 we show some details and results on this approach.

2.6 Elastic porous media: hybrid homogenization approach

Elastic porous media ~~has~~ been studied by Biot [20] ~~which~~ developed a model for the stresses wave propagation inside the solid matrix of a porous medium. His model has been a reference for elastic porous media with a close to unity density ratio (ρ_β/ρ_σ), as for the case of saturated soil.

Whitaker [148] has also approached the problem using the volume average method to homogenize ~~with~~ the solid and the fluid part. But the closure problems that came out from the averaging procedure of the solid equation are very difficult to solve. ~~Also there are no following studies that neither clarify the problem nor confirm the formulation.~~

The following works by Hussong et al. [74] and Wang et al. [145] showed how to extend the rigid case formulation of the VANS in case of elastic media. They show that the only term that has to be changed is the closure for the microscopic force (2.50). As a matter of fact the hypothesis of rigid porous media has been used in ~~with~~ the development of this term. They proposed a modification based on the physical interpretation of the microscopic force. In reality the force exerted by the fluid on the solid part has to take into account the solid velocity:

$$\mathbf{F}^M = -\nu_\beta \varepsilon \mathbf{H}^{-1} \cdot [\langle \mathbf{v}_\beta \rangle^\beta - \langle \mathbf{v}_\sigma \rangle^\beta];$$

the physics behind the force generation is the same and so it should be the formulation of the closure.

This simple modification can be included in a *hybrid homogenization approach*. As presented in paragraph 1.4, in order to describe the dynamic of a poroelastic layer we need a model for the fluid phase, one for the solid phase and an interface condition. ~~Nevertheless since the dynamics of the solid is usually computationally cheap there is no need to use an homogenized model for this part. Here we propose an approach that is independent from whatever solid model one wants to use. The pseudo-code to the macroscopic algorithm is the one~~

briefly outlined in algorithm 1, below.

```

Data:  $\langle \psi_\beta \rangle_n^\beta = \{\langle \mathbf{v}_\beta \rangle_n^\beta, \langle \mathbf{v}_\sigma \rangle_n^\beta, \langle p_\beta \rangle_n^\beta, \mathbf{H}_n, \varepsilon_n\}$ 
1 while  $t < T$  do
2    $n \rightarrow 0$ ;
3   while  $n < n_{max}$  do
4     Fluid solver VANS:  $\langle \mathbf{v}_\beta \rangle_{n+1}^\beta, \langle p_\beta \rangle_{n+1}^\beta$ 
5     Solid solver:  $\mathbf{v}_{\sigma n+1}$ 
6     Solid averaging:  $\varepsilon_{n+1}(x), \langle \mathbf{v}_\sigma \rangle_{n+1}^\beta$ 
7     Effective permeability metamodel:  $\mathbf{H}_{n+1} = f(\langle \mathbf{v}_\beta \rangle_{n+1}^\beta, \langle \mathbf{v}_\sigma \rangle_{n+1}^\beta)$ 
8     Relaxation:  $\langle \psi_\beta \rangle_{n+1}^\beta = (1 - \omega) \langle \psi_\beta \rangle_n^\beta + \omega \langle \psi_\beta \rangle_{n+1}^\beta$ 
9     if  $\|\langle \mathbf{v}_\beta \rangle_{n+1}^\beta - \langle \mathbf{v}_\beta \rangle_n^\beta\| < \epsilon$  then
10    | break;
11    else
12    |    $n = n + 1$ ;
13    end
14  end
15   $t = t + \Delta t$ ;
16   $\langle \psi_\beta \rangle_{n+1}^\beta = \langle \psi_\beta \rangle_{t+\Delta t}^\beta$ ;
17 end

```

Algorithm 1: Macroscopic algorithm for fluid-structure interaction of homogenized poroelastic medium.

Any solid model can be used in the model (for example Bernulli beam) and after its solution the new porosity field and homogenized solid velocity can be computed in the following manner:

$$\begin{aligned}\varepsilon &= \frac{1}{V} \int_{V_\beta} dV \\ \langle \mathbf{v}_\sigma \rangle^\beta &= \frac{1}{V} \int_{V_\sigma} \mathbf{v}_\sigma dV\end{aligned}$$

where V_σ is the solid part of the REV. The latter averaging procedure of the solid phase makes sense only in presence of multiple fibers in each REV or in case of non-rigid solids.

Using this approach with just some slight modification in the fluid equations, it is possible to easily develop a macroscopic algorithm that can take into account moving fibrous media. In the above algorithm we also introduce (in line 7) the concept of a metamodel for the apparent permeability. This model is needed since the effective permeability \mathbf{H} can be affected by the direction and intensity of the mean velocity field, as we show later in chapter 4. It is also worth noting that with the use of the penalization method (paragraph 2.5) the interface condition is implicitly treated in the above algorithm, and it is very simple

to implement even for moving porous media. Also, possible convergence and numerical instabilities of the algorithm can be controlled ~~numerical manner~~ with the relaxation parameter ω (Iron and Tuck [77]).

2.7 Note on the average of an average field

In the above sections we have briefly talked about the results in equation (2.6) that we recall here:

$$\langle \langle \psi_\beta \rangle |_r \rangle |_x = \langle \psi_\beta \rangle |_x$$

student — And introducing the decomposition (2.23) the above results can be used to state that the perturbation fields have ~~full~~ zero averaged:

$$\langle \tilde{\psi}_\beta \rangle = 0$$

student — But let's recall what the average operator really does when applied to an averaged quantities:

$$\langle \langle \psi_\beta \rangle |_r \rangle |_x = \frac{1}{V} \int_{V_\beta(x)} \langle \psi_\beta \rangle |_r(r) dV$$

student — The above equation can be described as the average computed over the volume V with centroid x , of the averaged field $\langle \psi_\beta \rangle |_r$ that can vary spatially, because of the change of r .

In order to show how the above expression can be simplified we expand the averaged quantity $\langle \psi_\beta \rangle |_r$ over the centroid x using Taylor's polynomial expansion:

$$\langle \psi_\beta \rangle |_r = \langle \psi_\beta \rangle |_x + \mathbf{y} \cdot \nabla \langle \psi_\beta \rangle |_x + \frac{1}{2} \mathbf{y} \mathbf{y} : \nabla \nabla \langle \psi_\beta \rangle |_x + O(\mathbf{y}^3)$$

Now if we put this expansion inside the averaging operator, we get:

$$\langle \langle \psi_\beta \rangle |_r \rangle |_x = \langle \psi_\beta \rangle |_x + \langle \mathbf{y} \rangle |_x \cdot \nabla \langle \psi_\beta \rangle |_x + \frac{1}{2} \langle \mathbf{y} \mathbf{y} \rangle |_x : \nabla \nabla \langle \psi_\beta \rangle |_x + O(\mathbf{y}^3)$$

The term $\langle \mathbf{y} \rangle$ is zero for REVs used in ordered porous media since they are always chosen to be symmetric around the REV centroid. The second term can be shown to be negligible either with the same length-scale constraint used in the REV definition, in fact Ochoa-Tapia and Whitaker [110], Paéz-García et al. [114] showed that this term is order $O(\epsilon^2)$. Although there is possible to choose an appropriate weight function that enforce $m * \mathbf{y} \mathbf{y} = 0$ strictly, these function are impractical (Davit and Quintard [40]). As we recall from section 2.3.3 the triangle shaped weight function almost satisfies this hypothesis. The function m^Δ guarantees a second order closure; this means that $\frac{1}{2} \langle \mathbf{y} \mathbf{y} \rangle |_x : \nabla \nabla \langle \psi_\beta \rangle |_x$ is a constant. Further manipulation can show that it is also negligible ($O(\epsilon^2)$).

2.8 Conclusions

We have shown in this chapter how to formally derive the homogenized version of the Navier-Stokes equations. We have also discussed the extension of the model in case of elastic porous medium. A lot of emphasis has been put on the closure problem for the microscopic force ~~since~~ the topic is further developed in chapter 4. Although the average volume method is not new we think that this chapter help to place in context the latest works in literature. The chapter also forms a basis for better understanding of the next chapters.

the
and

Bibliography

- [1] JD Ackerman and A Okubo. Reduced mixing in a marine macrophyte canopy. *Functional Ecology*, pages 305–309, 1993.
- [2] B.M. Adams, L.E. Bauman, W.J. Bohnhoff, K.R. Dalbey, M.S. Ebeida, J.P. Eddy, M.S. Eldred, P.D. Hough, K.T. Hu, J.D. Jakeman, J.A. Stephens, L.P. Swiler, D.M. Vigil, , and T.M. Wildey. Dakota, a multilevel parallel object-oriented framework for design optimization, parameter estimation, uncertainty quantification, and sensitivity analysis: Version 6.0 Theory Manual. Technical report, Sandia National Laboratories, SAND2014-4253, 2014.
- [3] Mehrez Agnaou, Didier Lasseux, and Azita Ahmadi. From steady to unsteady laminar flow in model porous structures: an investigation of the first Hopf bifurcation. *Computers & Fluids*, 136:67–82, 2016.
- [4] José Alvarado, Jean Comtet, Emmanuel de Langre, and A. E. Hosoi. Nonlinear flow response of soft hair beds. *Nature Physics*, 13:1014–1019, 2017.
- [5] Philippe Angot, Charles-Henri Bruneau, and Pierre Fabrie. A penalization method to take into account obstacles in incompressible viscous flows. *Numerische Mathematik*, 81(4):497–520, 1999.
- [6] Takashi Asaeda, Takeshi Fujino, and Jagath Manatunge. Morphological adaptations of emergent plants to water flow: a case study with *typha angustifolia*, *zizania latifolia* and *phragmites australis*. *Freshwater Biology*, 50(12):1991–2001, 2005.
- [7] Jean-Louis Auriault and E Sanchez-Palencia. Etude du comportement macroscopique d'un milieu poreux saturé déformable. *Journal de mécanique*, 16(4):575–603, 1977.
- [8] JL Auriault. Effective macroscopic description for heat conduction in periodic composites. *International Journal of Heat and Mass Transfer*, 26(6):861–869, 1983.
- [9] Jean Barrere, Olivier Gipouloux, and Stephen Whitaker. On the closure problem for darcy's law. *Transport in porous media*, 7(3):209–222, 1992.

- [10] Sylvie Barsu, Delphine Doppler, J John Soundar Jerome, Nicolas Rivière, and Michel Lance. Drag measurements in laterally confined 2d canopies: Reconfiguration and sheltering effect. *Physics of Fluids*, 28(10):107101, 2016.
- [11] Ilenia Battiato and Simonetta Rubol. Single-parameter model of vegetated aquatic flows. *Water Resources Research*, 50(8):6358–6369, 2014.
- [12] Michaël Baudin, Anne Dutfoy, Bertrand Iooss, and Anne-Laure Popelin. *OpenTURNS: An industrial software for uncertainty quantification in simulation*. Springer International Publishing, Cham, 2016. ISBN 978-3-319-11259-6. doi: 10.1007/978-3-319-11259-6_64-1. URL http://dx.doi.org/10.1007/978-3-319-11259-6_64-1.
- [13] Gordon S Beavers and Daniel D Joseph. Boundary conditions at a naturally permeable wall. *Journal of fluid mechanics*, 30(1):197–207, 1967.
- [14] Gordon S Beavers and Daniel D Joseph. Boundary conditions at a naturally permeable wall. *Journal of fluid mechanics*, 30(01):197–207, 1967.
- [15] DW Bechert, M Bruse, W Hage, and R Meyer. Biological surfaces and their technological application—laboratory and flight experiments on drag reduction and separation control. *AIAA paper*, 1960, 1997.
- [16] DW Bechert, M Bruse, W vd Hage, JG Th Van der Hoeven, and G Hoppe. Experiments on drag-reducing surfaces and their optimization with an adjustable geometry. *Journal of fluid mechanics*, 338:59–87, 1997.
- [17] Stephen E Belcher, Ian N Harman, and John J Finnigan. The wind in the willows: flows in forest canopies in complex terrain. *Annual Review of Fluid Mechanics*, 44: 479–504, 2012.
- [18] S Bhattacharyya and AK Singh. Reduction in drag and vortex shedding frequency through porous sheath around a circular cylinder. *International Journal for Numerical Methods in Fluids*, 65(6):683–698, 2011.
- [19] Bharat Bhushan. *Biomimetics: bioinspired hierarchical-structured surfaces for green science and technology*. Springer, 2016.
- [20] A Boomsma and F Sotiropoulos. Direct numerical simulation of sharkskin denticles in turbulent channel flow. *Physics of Fluids*, 28(3):035106, 2016.
- [21] Alessandro Bottaro, Peter Corbett, and Paolo Luchini. The effect of base flow variation on flow stability. *Journal of Fluid Mechanics*, 476:293–302, 2003.
- [22] WP Breugem, BJ Boersma, and RE Uittenbogaard. The influence of wall permeability on turbulent channel flow. *Journal of Fluid Mechanics*, 562:35–72, 2006.

- [23] W Brevis, M García-Villalba, and Y Niño. Experimental and large eddy simulation study of the flow developed by a sequence of lateral obstacles. *Environmental Fluid Mechanics*, 14(4):873–893, 2014.
- [24] HC Brinkman. A calculation of the viscous force exerted by a flowing fluid on a dense swarm of particles. *Applied Scientific Research*, 1(1):27–34, 1949.
- [25] Charles-Henri Bruneau and Iraj Mortazavi. Passive control of the flow around a square cylinder using porous media. *International Journal for Numerical Methods in Fluids*, 46(4):415–433, 2004.
- [26] Charles-Henri Bruneau and Iraj Mortazavi. Numerical modelling and passive flow control using porous media. *Computers & Fluids*, 37(5):488–498, 2008.
- [27] Charles-Henri Bruneau, Emmanuel Creusé, Delphine Depeyras, Patrick Gilliéron, and Iraj Mortazavi. Coupling active and passive techniques to control the flow past the square back ahmed body. *Computers & Fluids*, 39(10):1875–1892, 2010.
- [28] Dennis M Bushnell, Jerry N Hefner, and Robert L Ash. Effect of compliant wall motion on turbulent boundary layers. *The Physics of Fluids*, 20(10):S31–S48, 1977.
- [29] J-P Caltagirone. Sur l’interaction fluide-milieu poreux; application au calcul des efforts exercés sur un obstacle par un fluide visqueux. *Comptes rendus de l’Académie des sciences. Série II, Mécanique, physique, chimie, astronomie*, 318(5):571–577, 1994.
- [30] Claudio Canuto, M Yousuff Hussaini, Alfio Quarteroni, and Thomas A Zang. Spectral methods in fluid dynamics. Technical report, Springer, 1988.
- [31] Ruben G Carbonell and Stephen Whitaker. Heat and mass transfer in porous media. *Fundamentals of transport phenomena in porous media*, 82:121–198, 1984.
- [32] P. C. Carman. Fluid Flow Through Granular Beds. *Transactions - Institution of Chemical Engineers*, 15:150–166, 1937.
- [33] Peter W Carpenter. Status of transition delay using compliant walls. *Viscous drag reduction in boundary layers*, 123:79–113, 1990.
- [34] Rao Chen, Ikeda Teruaki, Nakata Toshiyuki, and Liu Hao. Owl-inspired leading-edge serrations play a crucial role in aerodynamic force production and sound suppression. *Bioinspiration & Biomimetics*, 12(4):046008, 2017.
- [35] Haecheon Choi, Parviz Moin, and John Kim. Direct numerical simulation of turbulent flow over riblets. *Journal of fluid mechanics*, 255:503–539, 1993.

- [36] William O Criminale, Thomas Luther Jackson, and Ronald Douglas Joslin. *Theory and computation of hydrodynamic stability*. Cambridge University Press, 2003.
- [37] Henry Darcy. *Les fontaines publiques de la ville de Dijon*. Victor Dalmont, 1856.
- [38] Yohan Davit and Michel Quintard. Technical notes on volume averaging in porous media i: How to choose a spatial averaging operator for periodic and quasiperiodic structures. *Transport in Porous Media*, 119(3):555–584, 2017.
- [39] Yohan Davit, Christopher G Bell, Helen M Byrne, Lloyd AC Chapman, Laura S Kimpton, Georgina E Lang, Katherine HL Leonard, James M Oliver, Natalie C Pearson, Rebecca J Shipley, et al. Homogenization via formal multiscale asymptotics and volume averaging: How do the two techniques compare? *Advances in Water Resources*, 62:178–206, 2013.
- [40] Emmanuel De Langre. Effects of wind on plants. *Annu. Rev. Fluid Mech.*, 40:141–168, 2008.
- [41] Brian Dean and Bharat Bhushan. Shark-skin surfaces for fluid-drag reduction in turbulent flow: a review. *Philosophical Transactions of the Royal Society of London A: Mathematical, Physical and Engineering Sciences*, 368(1929):4775–4806, 2010.
- [42] S Dupont, F Gosselin, Charlotte Py, Emmanuel De Langre, Pascal Hemon, and Yves Brunet. Modelling waving crops using large-eddy simulation: comparison with experiments and a linear stability analysis. *Journal of Fluid Mechanics*, 652:5–44, 2010.
- [43] James E Eckman. The role of hydrodynamics in recruitment, growth, and survival of argopecten irradians (l.) and anomia simplex (d'orbigny) within eelgrass meadows. *Journal of Experimental Marine Biology and Ecology*, 106(2):165–191, 1987.
- [44] DA Edwards, M Shapiro, P Bar-Yoseph, and M Shapira. The influence of Reynolds number upon the apparent permeability of spatially periodic arrays of cylinders. *Physics of Fluids A: Fluid Dynamics*, 2(1):45–55, 1990.
- [45] Sabri Ergun and Ao Ao Orning. Fluid flow through randomly packed columns and fluidized beds. *Industrial & Engineering Chemistry*, 41(6):1179–1184, 1949.
- [46] Julien Favier, Antoine Dauptain, Davide Basso, and Alessandro Bottaro. Passive separation control using a self-adaptive hairy coating. *Journal of Fluid Mechanics*, 627:451–483, 2009.
- [47] Julien Favier, Cuicui Li, Laura Kamps, Alistair Revell, Joseph O'Connor, and Christoph Brücker. The pelskin project—part i: fluid–structure interaction for a row of flexible flaps: a reference study in oscillating channel flow. *Meccanica*, 52(8):1767–1780, 2017.

- [48] John Finnigan. Turbulence in plant canopies. *Annual review of fluid mechanics*, 32(1):519–571, 2000.
- [49] PH Forchheimer. Wasserbewegung durch boden. *Zeitz. Ver. Duetch Ing.*, 45:1782–1788, 1901.
- [50] Maria Cristina Gambi, Arthur RM Nowell, and Peter A Jumars. Flume observations on flow dynamics in *zostera marina* (eelgrass) beds. *Marine ecology progress series*, pages 159–169, 1990.
- [51] Ricardo García-Mayoral and Javier Jiménez. Drag reduction by riblets. *Philosophical Transactions of the Royal Society of London A: Mathematical, Physical and Engineering Sciences*, 369(1940):1412–1427, 2011.
- [52] Ricardo García-Mayoral and Javier Jiménez. Hydrodynamic stability and breakdown of the viscous regime over riblets. *Journal of Fluid Mechanics*, 678:317–347, 2011.
- [53] M Ghisalberti and HM Nepf. The limited growth of vegetated shear layers. *Water Resources Research*, 40(7), 2004.
- [54] Marco Ghisalberti. Obstructed shear flows: similarities across systems and scales. *Journal of Fluid Mechanics*, 641:51–61, 2009.
- [55] Marco Ghisalberti and Heidi Nepf. Mass transport in vegetated shear flows. *Environmental fluid mechanics*, 5(6):527–551, 2005.
- [56] Marco Ghisalberti and Heidi M Nepf. Mixing layers and coherent structures in vegetated aquatic flows. *Journal of Geophysical Research: Oceans*, 107(C2), 2002.
- [57] Anthony A Giunta, Steven F Wojtkiewicz, and Michael S Eldred. Overview of modern design of experiments methods for computational simulations. In *Proceedings of the 41st AIAA aerospace sciences meeting and exhibit, AIAA-2003-0649*, 2003.
- [58] giuseppe ... sfera 3d porosa. *JFM*, 2017. *METTI IL RIF. COME "SUBMITTED"*
- [59] G. Gomez-de Segura, A. Sharma, and R. Garcia-Mayoral. Turbulent drag reduction by anisotropic permeable coatings. In *10th International Symposium on Turbulence and Shear Flow Phenomena*, 2017.
- [60] F Gosselin and Emmanuel De Langre. Destabilising effects of plant flexibility in air and aquatic vegetation canopy flows. *European Journal of Mechanics-B/Fluids*, 28(2):271–282, 2009.
- [61] Frédéric P Gosselin and Emmanuel De Langre. Drag reduction by reconfiguration of a poroelastic system. *Journal of Fluids and Structures*, 27(7):1111–1123, 2011.

- [62] William G Gray. A derivation of the equations for multi-phase transport. *Chemical Engineering Science*, 30(2):229–233, 1975.
- [63] Luca Grizzetti, Maurizio Quadrio, and Luca Cortelezzi. Studio sperimentale della scia di un corpo tozzo in presenza di inserti di materiale poroso. Master’s thesis, Politecnico di Milano: Dipartimento Ingegneria Aerospaziale, 2015.
- [64] Raymond E Grizzle, Frederick T Short, Carter R Newell, Heidi Hoven, and Linda Kindblom. Hydrodynamically induced synchronous waving of seagrasses: ‘monami’ and its possible effects on larval mussel settlement. *Journal of Experimental Marine Biology and Ecology*, 206(1-2):165–177, 1996.
- [65] AM Hamed, MJ Sadowski, HM Nepf, and LP Chamorro. Impact of height heterogeneity on canopy turbulence. *Journal of Fluid Mechanics*, 813:1176–1196, 2017.
- [66] AF Heenan and JF Morrison. Passive control of pressure fluctuations generated by separated flow. *AIAA journal*, 36(6):1014–1022, 1998.
- [67] M Yousuff Hussaini and Thomas A Zang. Spectral methods in fluid dynamics. *Annual review of fluid mechanics*, 19(1):339–367, 1987.
- [68] Jeanette Hussong, Wim-Paul Breugem, and Jerry Westerweel. A continuum model for flow induced by metachronal coordination between beating cilia. *Journal of Fluid Mechanics*, 684:137–162, 2011.
- [69] Syunsuke Ikeda and Minoru Kanazawa. Three-dimensional organized vortices above flexible water plants. *Journal of Hydraulic Engineering*, 122(11):634–640, 1996.
- [70] E Inoue. Studies of the phenomena of waving plants (“honami”) caused by wind. *Journal of Agricultural Meteorology*, 11(3):87–90, 1955.
- [71] Motoyuki Itoh, Shinji Tamano, Ryo Iguchi, Kazuhiko Yokota, Norio Akino, Ryutaro Hino, and Shinji Kubo. Turbulent drag reduction by the seal fur surface. *Physics of Fluids*, 18(6):065102, 2006.
- [72] Justin W Jaworski and N Peake. Aerodynamic noise from a poroelastic edge with implications for the silent flight of owls. *Journal of Fluid Mechanics*, 723:456–479, 2013.
- [73] Javier Jimenez, Markus Uhlmann, Alfredo Pinelli, and Genta Kawahara. Turbulent shear flow over active and passive porous surfaces. *Journal of Fluid Mechanics*, 442:89–117, 2001.

- [74] Matthew P Juniper, Ardeshir Hanifi, and Vassilios Theofilis. Modal stability theory lecture notes from the flow-nordita summer school on advanced instability methods for complex flows, stockholm, sweden, 2013. *Applied Mechanics Reviews*, 66(2):024804, 2014.
- [75] Katharina Klausmann and Bodo Ruck. Drag reduction of circular cylinders by porous coating on the leeward side. *Journal of Fluid Mechanics*, 813:382–411, 2017.
- [76] Jack P.C. Kleijnen. Regression and kriging metamodels with their experimental designs in simulation: A review. *European Journal of Operational Research*, 256(1):1 – 16, 2017. ISSN 0377-2217. doi: <https://doi.org/10.1016/j.ejor.2016.06.041>.
- [77] J Kozeny. Über grundwasserbewegung. *Wasserkraft und Wasserwirtschaft*, 22(5):67–70, 1927.
- [78] Uģis Lācis, Giuseppe Antonio Zampogna, and Shervin Bagheri. A computational continuum model of poroelastic beds. In *Proc. R. Soc. A*, volume 473, page 20160932. The Royal Society, 2017.
- [79] Amy Lang, Michael T Bradshaw, Jonathon A Smith, Jennifer N Wheelus, Philip Motta, Maria Habegger, and Robert E Hueter. Movable shark scales act as a passive dynamic micro-roughness to control flow separation. *Bioinspiration & Biomimetics*, 9:036017, 07 2014.
- [80] Didier Lasseux, A. Arani Abbasian, and A. Ahmadi. On the stationary macroscopic inertial effects for one phase flow in ordered and disordered porous media. *Physics of Fluids (1994-present)*, 23(7):073103, 2011.
- [81] Michael Le Bars and M Grae Worster. Interfacial conditions between a pure fluid and a porous medium: implications for binary alloy solidification. *Journal of Fluid Mechanics*, 550:149–173, 2006.
- [82] Geoffrey M Lilley. A study of the silent flight of the owl. *AIAA paper*, 2340(1998):1–6, 1998.
- [83] Paolo Luchini, Fernando Manzo, and Amilcare Pozzi. Resistance of a grooved surface to parallel flow and cross-flow. *Journal of fluid mechanics*, 228:87–109, 1991.
- [84] Nicola Luminari, Christophe Airiau, and Alessandro Bottaro. Drag-model sensitivity of kelvin-helmholtz waves in canopy flows. *Physics of Fluids*, 28(12):124103, 2016.
- [85] Timothy I Marjoribanks, Richard J Hardy, Stuart N Lane, and Daniel R Parsons. Does the canopy mixing layer model apply to highly flexible aquatic vegetation? insights from numerical modelling. *Environmental Fluid Mechanics*, 17(2):277–301, 2017.

k H

- [86] Samuel Martin and Bharat Bhushan. Discovery of ripples in a bird beak (ryncrops) for low fluid drag. *Philosophical Transactions of the Royal Society of London A: Mathematical, Physical and Engineering Sciences*, 374(2073), 2016. ISSN 1364-503X. doi: 10.1098/rsta.2016.0134.
- [87] Maria Maza, Javier L Lara, and Inigo J Losada. A coupled model of submerged vegetation under oscillatory flow using navier–stokes equations. *Coastal Engineering*, 80:16–34, 2013.
- [88] Maria Maza, Javier L Lara, and Inigo J Losada. Tsunami wave interaction with mangrove forests: A 3-d numerical approach. *Coastal Engineering*, 98:33–54, 2015.
- [89] Doug McLean. *Understanding aerodynamics: arguing from the real physics*. John Wiley & Sons, 2012.
- [90] CC Mei and J-L Auriault. The effect of weak inertia on flow through a porous medium. *Journal of Fluid Mechanics*, 222:647–663, 1991.
- [91] Chiang C Mei and Bogdan Vernescu. *Homogenization methods for multiscale mechanics*. World scientific, 2010.
- [92] Andro Mikelić and Willi Jäger. On the interface boundary condition of beavers, joseph, and saffman. *SIAM Journal on Applied Mathematics*, 60(4):1111–1127, 2000.
- [93] Chloé Mimeau, Iraj Mortazavi, and G-H Cottet. Passive control of the flow around a hemisphere using porous media. *European Journal of Mechanics-B/Fluids*, 65: 213–226, 2017.
- [94] Philip Motta, Maria Habegger, Amy Lang, Robert Hueter, and Jessica Davis. Scale morphology and flexibility in the shortfin mako *isurus oxyrinchus* and the blacktip shark *carcharhinus limbatus*. *Journal of morphology*, 273, 10 2012.
- [95] Hiroshi Naito and Koji Fukagata. Numerical simulation of flow around a circular cylinder having porous surface. *Physics of Fluids*, 24(11):117102, 2012.
- [96] Heidi M Nepf. Flow and transport in regions with aquatic vegetation. *Annual Review of Fluid Mechanics*, 44:123–142, 2012.
- [97] J Alberto Ochoa-Tapia, Francisco José Valdés-Parada, Benoît Goyeau, and Didier Lasseux. Fluid motion in the fluid/porous medium inter-region. *Revista Mexicana de Ingeniería Química*, 16(3):923–938, 2017.
- [98] Johannes Oeffner and George V. Lauder. The hydrodynamic function of shark skin and two biomimetic applications. *Journal of Experimental Biology*, 215(5):785–795, 2012. ISSN 0022-0949. doi: 10.1242/jeb.063040.

- [99] Catherine Teresa Paéz-García, Francisco J Valdés-Parada, and Didier Lasseux. Macroscopic momentum and mechanical energy equations for incompressible single-phase flow in porous media. *Physical Review E*, 95(2):023101, 2017.
- [100] S Patil and VP Singh. Characteristics of monami wave in submerged vegetated flow. *Journal of Hydrologic Engineering*, 15(3):171–181, 2010.
- [101] M. Pauthenet, Y. Davit, M. Quintard, and A Bottaro. Topological scaling for inertial transition in porous media. *submitted*, 2017.
- [102] Alfredo Pinelli, Mohammad Omidyeganeh, Christoph Brücker, Alistair Revell, Abhishek Sarkar, and Edoardo Alinovi. The pelskin project: part iv—control of bluff body wakes using hairy filaments. *Meccanica*, 52(7):1503–1514, 2017.
- [103] Charlotte Py, Emmanuel De Langre, and Bruno Moulia. The mixing layer instability of wind over a flexible crop canopy. *Comptes Rendus Mécanique*, 332(8):613–618, 2004.
- [104] Charlotte Py, Emmanuel De Langre, and Bruno Moulia. A frequency lock-in mechanism in the interaction between wind and crop canopies. *Journal of Fluid Mechanics*, 568:425–449, 2006.
- [105] Michel Quintard and Stephen Whitaker. Transport in ordered and disordered porous media i: The cellular average and the use of weighting functions. *Transport in Porous Media*, 14(2):163–177, 1994.
- [106] Michel Quintard and Stephen Whitaker. Transport in ordered and disordered porous media ii: Generalized volume averaging. *Transport in porous media*, 14(2):179–206, 1994.
- [107] KR Rajagopal. On a hierarchy of approximate models for flows of incompressible fluids through porous solids. *Mathematical Models and Methods in Applied Sciences*, 17(02):215–252, 2007.
- [108] M_R Raupach, JJ Finnigan, and Y Brunet. Coherent eddies and turbulence in vegetation canopies: the mixing-layer analogy. In *Boundary-Layer Meteorology 25th Anniversary Volume, 1970–1995*, pages 351–382. Springer, 1996.
- [109] Alistair Revell, Joseph O'Connor, Abhishek Sarkar, Cuicui Li, Julien Favier, Laura Kamps, and Christoph Brücker. The pelskin project: part ii—investigating the physical coupling between flexible filaments in an oscillating flow. *Meccanica*, 52(8):1781–1795, 2017.
- [110] P.J. Roache. *Verification and validation in computational science and engineering*. Hermosa Press, Albuquerque, NM., 1998.

- [111] Marco E Rosti, Laura Kamps, Christoph Bruecker, Mohammad Omidyeganeh, and Alfredo Pinelli. The pelskin project-part v: towards the control of the flow around aerofoils at high angle of attack using a self-activated deployable flap. *Meccanica*, 52(8):1811–1824, 2017.
- [112] Peter J Schmid and Dan S Henningson. *Stability and transition in shear flows*, volume 142. Springer Science & Business Media, 2012.
- [113] Antonio Segalini, Jens HM Fransson, and P Henrik Alfredsson. An experimental analysis of canopy flows. In *Journal of Physics: Conference Series*, volume 318, page 072018. IOP Publishing, 2011.
- [114] Antonio Segalini, Jens HM Fransson, and P Henrik Alfredsson. Scaling laws in canopy flows: a wind-tunnel analysis. *Boundary-layer meteorology*, 148(2):269–283, 2013.
- [115] Ravi Singh, MM Bandi, Amala Mahadevan, and Shreyas Mandre. Linear stability analysis for monami in a submerged seagrass bed. *Journal of Fluid Mechanics*, 786, 2016.
- [116] E Skjetne and JL Auriault. New insights on steady, non-linear flow in porous media. *European Journal of Mechanics-B/Fluids*, 18(1):131–145, 1999.
- [117] Nathan Slegers, Michael Heilman, Jacob Cranford, Amy Lang, John Yoder, and Maria Laura Habegger. Beneficial aerodynamic effect of wing scales on the climbing flight of butterflies. *Bioinspiration & Biomimetics*, 12(1):016013, 2017.
- [118] Cyprien Soulaine and Michel Quintard. On the use of a Darcy–Forchheimer like model for a macro-scale description of turbulence in porous media and its application to structured packings. *International Journal of Heat and Mass Transfer*, 74:88–100, 2014.
- [119] RB Srygley and ALR Thomas. Unconventional lift-generating mechanisms in free-flying butterflies. *Nature*, 420(6916):660, 2002.
- [120] Emmanuel Stratakis, Vassilia Zorba, Marios Barberoglou, Emmanuel Spanakis, Sophia Rhizopoulou, Panagiotis Tzanetakis, Spiros Anastasiadis, and Costas Fotakis. Laser structuring of water-repellent biomimetic surfaces. *SPIE Newsroom*, 10(2.1200901):1441, 2009.
- [121] Nils Tilton and Luca Cortelezzi. Linear stability analysis of pressure-driven flows in channels with porous walls. *Journal of Fluid Mechanics*, 604:411–445, 2008.
- [122] Cameron Tropea and Horst Bleckmann. *Nature-Inspired Fluid Mechanics: Results of the DFG Priority Programme 1207 "Nature-inspired Fluid Mechanics" 2006-2012*, volume 119. Springer Science & Business Media, 2012.

O HEM SEMPRE IL NOME PER INTERO
OPPURE SEMPRE (E SOLO) LE INIZIALI...

- [123] Divya Venkataraman and Alessandro Bottaro. Numerical modeling of flow control on a symmetric aerofoil via a porous, compliant coating. *Physics of Fluids*, 24(9):093601, 2012.
- [124] H. G. Weller, G. Tabor, H. Jasak, and C. Fureby. A tensorial approach to computational continuum mechanics using object-oriented techniques. *Computers in Physics*, 12(6):620–631, 1998.
- [125] Stephen Whitaker. The transport equations for multi-phase systems. *Chemical Engineering Science*, 28(1):139–147, 1973.
- [126] Stephen Whitaker. Flow in porous media i: A theoretical derivation of darcy's law. *Transport in Porous Media*, 1(1):3–25, 1986.
- [127] Stephen Whitaker. Flow in porous media iii: deformable media. *Transport in Porous Media*, 1(2):127–154, 1986.
- [128] Stephen Whitaker. The Forchheimer equation: a theoretical development. *Transport in Porous Media*, 25(1):27–61, 1996.
- [129] Stephen Whitaker. *The Method of Volume Averaging*, volume 13. Springer Science & Business Media, 2013.
- [130] K Yazdchi, S Srivastava, and S Luding. Microstructural effects on the permeability of periodic fibrous porous media. *International Journal of Multiphase Flow*, 37(8):956–966, 2011.
- [131] G. A. Zampogna and A. Bottaro. Fluid flow over and through a regular bundle of rigid fibres. *Journal of Fluid Mechanics*, 792:5–35, 2016. doi: 10.1017/jfm.2016.66.
- [132] Giuseppe A Zampogna and Alessandro Bottaro. Fluid flow over and through a regular bundle of rigid fibres. *Journal of Fluid Mechanics*, 792:5–35, 2016.
- [133] Giuseppe A Zampogna and Alessandro Bottaro. private communication. *The values of \mathcal{K}_{11} and \mathcal{K}_{22} arise from the solution of a local, microscopic problem which accounts for inertia through the porous medium [132]. It is not unexpected that \mathcal{K}_{11} approaches \mathcal{K}_{22} as we leave the Stokes regime.*, 2016.
- [134] Giuseppe A Zampogna and Alessandro Bottaro. The pelskin project—part iii: a homogenized model of flows over and through dense poroelastic media. *Meccanica*, 52(8):1797–1808, 2017.
- [135] Giuseppe A Zampogna and Alessandro Bottaro. The pelskin project—part iii: A homogenized model of flows over and through dense poroelastic media. *Meccanica*, 52(8):1797–1808, 2017.

- [136] Giuseppe A Zampogna, Franck Pluvinage, Azeddine Kourta, and Alessandro Bottaro. Instability of canopy flows. *Water Resources Research*, 52(7):5421–5432, 2016.
- [137] Xueyan Zhang and Heidi M Nepf. Exchange flow between open water and floating vegetation. *Environmental fluid mechanics*, 11(5):531–546, 2011.

Appendix A: Kriging metamodel

sempre K MINUSCOLA

Introduction

The Kriging metamodel technique has already been introduced in chapter 4; however, to complete the description of the method, the numerical procedure and some implementation examples are presented in this appendix.

The Kriging method was invented to get prediction of missing geostatistics data (Krige [90]). However, this methodology has been further generalized and applied extensively to build metamodels for a large variety of applications. The method can treat highly non linear output of an experiment and can be used to either interpolate or extrapolate responses from a sample set.

In this discussion ~~the~~ $\hat{f}(\chi)$ is a model for the true function $f(\chi)$ and \hat{y} is the model prediction of the true response $y = f(\chi)$ that is evaluated at the point χ .

After the exploration of the design possibilities the database produced is usually organized as a set $(\mathbf{x}_i, y(\mathbf{x}_i))$ $i = 1, \dots, n$ where

- \mathbf{x}_i is the i -th vector element containing the k input parameters for the i -th experiment realization
- y_i is the scalar response of the experiment for the vector of inputs \mathbf{x}_i ³
- χ is the new input vector for which we seek the approximate output $\hat{y} = \hat{f}(\chi)$

Mathematical modelling

We define with ~~provided that~~ n is the number of points in the sample design set and k is the number of inputs of the experiment; the $n \times k$ matrix containing all the inputs is indicated with \mathbf{X} and the $n \times 1$ vector containing all the responses is indicated as \mathbf{Y} .

The Kriging response for a new input point χ is given by the linear predictor:

$$\hat{y} = \hat{f}(\chi) = \sum_{i=1}^N \lambda_i(\chi) f(\mathbf{x}_i) = \sum_{i=1}^N \lambda_i(\chi) y_i \quad (5.7)$$

³ y_i is always a scalar because even in case of multiple output for an experiment ~~they~~ they are supposed to be uncorrelated. It means that if we had p elements in each \mathbf{y}_i we would have to build p metamodels.

Unbiased \hat{y} is considered to be a new realization of the random Gaussian process that has generated the set of responses \mathbf{Y} . The weights λ_i are the solution of a linear system obtained by minimizing the variance of the error between the predictor and the random process. The best *linear unbiased predictor* BLUP is obtained finding the weights λ_i that minimize:

$$MSE[\hat{y}(\chi)] = E \left[(\hat{f}(\chi) - f(\chi))^2 \right] = E \left[(\boldsymbol{\lambda}^T(\chi) \mathbf{Y} - y(\chi))^2 \right], \quad (5.8)$$

Unbiased under the unbiasedness condition:

$$E \left[\hat{f}(\chi) - f(\chi) \right] = E \left[\boldsymbol{\lambda}^T(\chi) \mathbf{Y} - y(\chi) \right] = 0 \quad (5.9)$$

This relation means that the predictor and the Gaussian process have the same mean value for every new point χ .

The equation (5.9) is further developed yielding:

$$E \left[\hat{f}(\chi) - f(\chi) \right] = \boldsymbol{\lambda}^T \chi E[f(\mathbf{X})] - E[f(\chi)] = \sum_{i=1}^n \lambda_i(\chi) \mu(\mathbf{x}_i) - \mu(\chi) = 0 \quad (5.10)$$

where $\mu(\chi)$ is the mean value of the true function at the point χ , instead $\mu(\mathbf{x}_i)$ is the mean of all the realizations collected for the database.

Different types of Kriging approximation exist according to how $\mu(\chi)$ is evaluated:

- simple Kriging assume that the trend has null value: $\mu(\chi) = 0$
- ordinary Kriging assume that the trend is an unknown constant: $\mu(\chi) = \mu$
- universal Kriging assume that the trend is the solution of a generalized least squares model in which it is possible to decide the order (n_β) ⁴ of the chosen base: $\mu(\chi) = \mathbf{g}^T(\chi) \boldsymbol{\beta}$, where $\mathbf{g}(\chi)$ is the base evaluation at the point χ and the vector $\boldsymbol{\beta}$ contains the n_β coefficients of the model.

The unbiased condition (5.10) can be so rewritten, without loss of generality:

$$\boldsymbol{\lambda}^T(\chi) \mathbf{G}(\mathbf{X}) \boldsymbol{\beta} - \mathbf{g}^T(\chi) \boldsymbol{\beta} = 0 \implies \boldsymbol{\lambda}^T(\chi) \mathbf{G}(\mathbf{X}) = \mathbf{g}^T(\chi) \quad (5.11)$$

where $\mathbf{G}(\mathbf{X})$ is the $n \times n_\beta$ matrix containing the evaluation of the least squared basis functions at all points in \mathbf{X} .

⁴ It means that, for example, taking $n_\beta = 2$ the least squared model is quadratic.

Also the relation (5.8) can be manipulated:

$$\begin{aligned}
E \left[(\hat{f}(\chi) - f(\chi))^2 \right] &= var(\hat{f}(\chi) - f(\chi)) \\
&= var(\hat{f}(\chi)) + var(f(\chi)) - 2 cov(\hat{f}(\chi), f(\chi)) \\
&= var\left(\sum_{i=1}^n \lambda_i(\chi) f(x_i)\right) + var(f(\chi)) - 2 cov\left(\sum_{i=1}^n \lambda_i(\chi) f(x_i), f(\chi)\right) \\
&= \sum_{i=1}^n \sum_{j=1}^n \lambda_i(\chi) \lambda_j(\chi) cov(f(x_i), f(x_j)) + var(f(\chi)) \\
&\quad - 2 \sum_{i=1}^n \lambda_i(\chi) cov(f(x_i), f(\chi)) \\
&= \sum_{i=1}^n \sum_{j=1}^n \lambda_i(\chi) \lambda_j(\chi) cov(x_i, x_j) + var(f(\chi)) \\
&\quad - 2 \sum_{i=1}^n \lambda_i(\chi) cov(x_i, \chi) \quad (5.12)
\end{aligned}$$

where $\mathbf{c} = cov(\mathbf{X}, \chi)$ is the vector containing the estimated covariance between each point in the input set \mathbf{X} and the point χ for which we search the estimator. Similarly, $\mathbf{C}_{ij} = cov(x_i, x_j)$ represents the elements in the $n \times n$ matrix containing the correlation estimates between each point in \mathbf{X} .

Possible estimation for the two covariance matrixies are listed in the next section.

The derivative of the relation (5.12) with respect to λ is posed equal to zero in order to minimize the Kriging error, yielding the final relation:

$$\lambda^T(\chi) \mathbf{C} = \mathbf{c} \quad (5.13)$$

Introducing the Lagrangian multiplier ϕ for the unbiased constraint it is possible to build the partitioned matrix for the Kriging metamodel:

$$\begin{pmatrix} \mathbf{0} & \mathbf{G}^T \\ \mathbf{G} & \mathbf{C} \end{pmatrix} \begin{pmatrix} \phi \\ \lambda \end{pmatrix} = \begin{pmatrix} \mathbf{g} \\ \mathbf{c} \end{pmatrix} \quad (5.14)$$

Inherent Then, by inverting the partitioned matrix the Kriging predictor can be written as:

$$\hat{y}(\chi) = \mathbf{g}^T(\chi) \beta + \mathbf{c}^T(\chi) \mathbf{R}^{-1} (\mathbf{Y} - \mathbf{G} \beta) \quad (5.15)$$

The first term $\mathbf{g}(\chi)^T \beta$ is usually called *trend function* and the second term is the *Gaussian error model*. As a matter of fact, $(\mathbf{Y} - \mathbf{G} \beta)$ is the known vector of differences between the true outputs and the trend function at all the points \mathbf{X} in the database.

One of the Kriging metamodel benefits is that the model is exact at the data points. However, if it is known that the experiment realization used in the database present some reliability issue and/or have noise⁵, there is a technique that permits to take into account these effect. Adding a *nugget* (η) to all entries on the covariance matrix $\mathbf{C}^* = \mathbf{C} + \eta \mathbf{I}$ the metamodel is no more exact at the data points. The same technique is used to increase the conditioning number of the portioned system when dealing with numerical problems.

Covariance matrix choice

In order to give some indication on the choice of the proper covariance function let us first introduce the *semivariogram* concept. The semivariogram γ between two generic points, in the design space $\mathbf{x}_1, \mathbf{x}_2$, is defined as:

$$\gamma(\mathbf{x}_1, \mathbf{x}_1) = \frac{1}{2} E \left[(f(\mathbf{x}_1) - \mu(\mathbf{x}_1) - f(\mathbf{x}_2) + \mu(\mathbf{x}_2))^2 \right] \quad (5.16)$$

$$= \frac{1}{2} \text{var}(f(\mathbf{x}_1) - f(\mathbf{x}_2))$$

$$= \frac{1}{2} \text{var}(f(\mathbf{x}_1)) + \frac{1}{2} \text{var}(f(\mathbf{x}_2)) - \text{cov}(\mathbf{x}_1, \mathbf{x}_2) \quad (5.17)$$

The semivariogram for each datapoint in the database can be directly computed from the equation (5.16) and afterwards the relation (5.17) can be used to fit the semivariogram data with the covariance function.

Lets us clarify the last statements with an example. We chose to replicate the example present in Cavazzuti [38] in which the author propose an experiment that depends on two variables x_1 and x_2 and 10 realization^s. The experiment database is shown in figure 5.10.

The semivariogram functions, as a function of the Euclidian distance between the two points $h_{ij} = |\mathbf{x}_i - \mathbf{x}_j|$, has been computed using the equation (5.16) and is represented in figure 5.11 on the left. The points in the semivariogram are then averaged over a distance step whose width is equal to 0.25 and the points are shown on the right of figure 5.11. The correlation function should be chosen to be the best fit for the averaged semivariogram. This means that in theory, depending on the dataset, one could formulate ~~their own~~ a personalized covariance model.

What is done in practice is that some parametric families of correlation function^s has been proposed in literature; for example the *power exponential* correlation function reads:

$$c(\mathbf{x}_i, \mathbf{x}_j) = \sigma^2 \exp \left(- \sum_{k=1}^K \theta_k |x_{i,k} - x_{j,k}|^\nu \right). \quad (5.18)$$

The kriging predictor surfaces can show different behaviors for different selections of the above three parameters (σ , ν and θ) and their setting is thus crucial. The coefficient σ

⁵common in experimental data

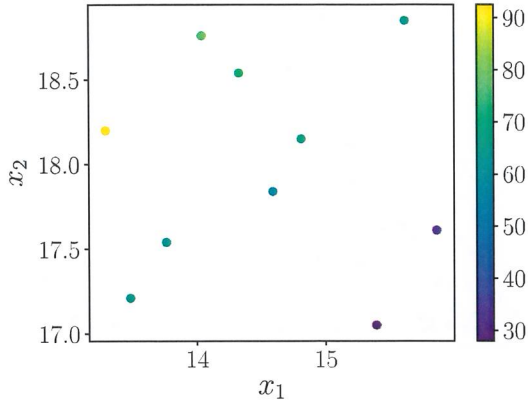


Figure 5.10: Experiment data points for the 10 realizations available. The color map represents the output realizations \mathbf{Y} of the experiment $f(\mathbf{X})$.

is an amplitude parameter for the correlation function. It determine variation of function \hat{f} from its mean. Small value of σ characterizes functions that stay close to their mean value, larger values allow more variation. It basically controls the gradient steepness around the data points. The exponent ν of the model has similar effects. The vector $\boldsymbol{\theta} = (\theta_{x_1}, \theta_{x_2})$ is a length scale parameter for the distance $|\mathbf{x}_i - \mathbf{x}_j|$, describes how smooth a function is. Small length scale values mean that function values can change quickly generating narrow bumps near the data points. Large values characterize functions that change only slowly but it will make the surface explode outside the convex hull described by the data points. It is possible to specify different length scales in different directions, in this manner the metamodel can include anisotropic effect for each variable of the experiment. This model has been fitted in the previous semivariogram choosing $\nu = 2$, $\theta = 1.895$ and $\sigma = 38.44$ and it is depicted in the right figure 5.11 using a red line. Is possible to see that this model fits well the data points for this experiment.

Another popular model for the covariance function is the *Matérn model*⁶ that reads:

$$c(\mathbf{x}_i, \mathbf{x}_j) = \sigma^2 \frac{2^{1-\nu}}{\Gamma(\nu)} \sum_{j=1}^k \left[\left(\frac{\sqrt{2\nu} |x_{i,k} - x_{j,k}|}{\theta_k} \right)^\nu \mathcal{K}_\nu \left(\frac{\sqrt{2\nu} |x_{i,k} - x_{j,k}|}{\theta_k} \right) \right] \quad (5.19)$$

where $\mathcal{K}_\nu(\cdot)$ is a modified Bessel function and $\Gamma(\cdot)$ is the gamma function. The parameters that can be used to tune the metamodel are the amplitude parameter σ , the exponent ν and the scale vector $\boldsymbol{\theta}$ with the same meaning as in the previous correlation function.

To summarize, when choosing the correlation it should be kept in mind:

- to well approximate the trend of the averaged semivariogram

⁶the one used in chapter 4

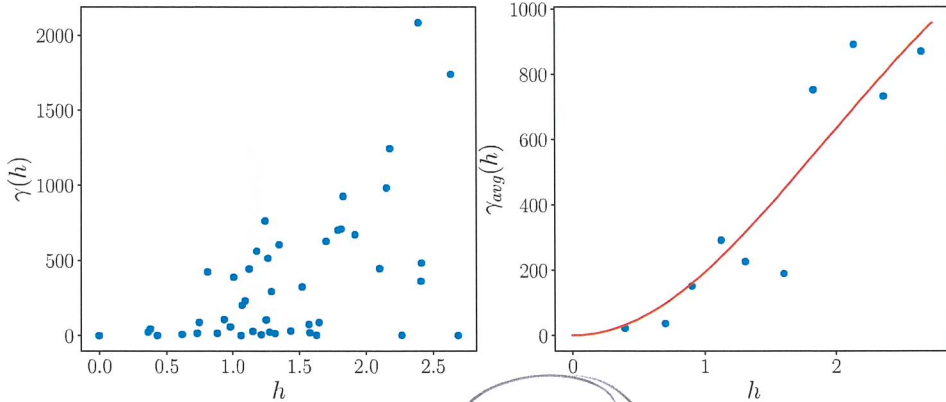


Figure 5.11: Left: Semivariogram versus the Euclidean distance computed for each data point against all the other. Right: The blue dots represent the same semivariogram on the left but averaged over a step of distance equal to 0.25. The red line corresponds to the semivariogram computed using the relation (5.17) with the covariance model power exponential with parameters $\nu = 2$, $\theta = 1.895$ and $\sigma = 38.44$.

- The scale parameter θ highly changes the presence of spurious minima and maxima in the metamodel. The others parameters ν , σ and η control the gradient and the exactness of the model around the data points.

Some examples of the response surface built with the above parameters are presented in the next section, along with the actual implementation.

Implementation example

An example of the implementation of Kriging algorithm is presented in the following. To build the model we use the open source library openTURNS (Baudin et al. [13]) using its Python application programming interface⁷. This interface has been chosen because it is very expressive even to non programmers. The code is shown in the listing below where each line is commented and is self explanatory. From line 1 through 22 the experiment database is created, in line 24 the trend function model is set constant but line 26 and 28 show how to set linear and quadratic least square trends. The covariance model is set in line 31, and from line 35 to 42 the algorithm metamodel tree is built and executed. At the end, is possible to get a callable function on the desired new point, line 44-47.

⁷although the crunching number computation is performed under the hood with C++

```

1 import numpy as np # import the generic vector library
2 import openturns as ot # import the openTURNS library
3
4 # define the k input variables as a n dimensional array
5 x1 = np.array([14.04, 14.33, 15.39, 13.76, 14.59,
6 13.48, 15.86, 15.61, 13.29, 14.81])
7 x2 = np.array([18.76, 18.54, 17.05, 17.54, 17.84,
8 17.21, 17.61, 18.85, 18.20, 18.15])
9
10 # transform the inputs as a n by k array
11 x = np.column_stack((x1, x2))
12
13 # define the outputs as a n by 1 array
14 y = np.array([[10],[2],[4],[-2],[9],[3],[0], [-1]])
15
16 # tranform the array in OT samples
17 X = ot.Sample(x)
18 Y = ot.Sample(y)
19
20 # explicit define the number of input i.e the k number
21 dimension = len(x[0])
22
23 # define the constant trend function
24 basis = ot.ConstantBasisFactory(dimension).build()
25 # or the linear trend
26 # basis = ot.LinearBasisFactory(dimension).build()
27 # or the quadratic trend
28 # basis = ot.QuadraticBasisFactory(dimension).build()
29
30 # select the covariance model squared exponential (sigma, theta)
31 covarianceModel = ot.SquaredExponential([38.44], [1.895])
32 # or define the Matern model
33 # covarianceModel = ot.MaternModel()
34
35 algo = ot.KrigingAlgorithm(X, Y, covarianceModel, basis) # build the metamodel
36
37 # eta = 0.2
38 # algo.setNoise([eta]*len(y)) # set the optional nugget
39
40 algo.run() # run the metamodel tree computation
41 result = algo.getResult() # return a container for the results

```

```
42     metamodel = result.getMetaModel() # get a callable function
43
44     # set the new point to compute
45     chi = np.array([13, 17])
46     # get the metamodel prediction for the point chi
47     y_chi = np.array(metamodel(chi))
```

It is possible to pass directly a vector of new points to the function `metamodel` in line 44. Figures 5.12, 5.13 and 5.14 show some metamodel surfaces with different parameters setup.

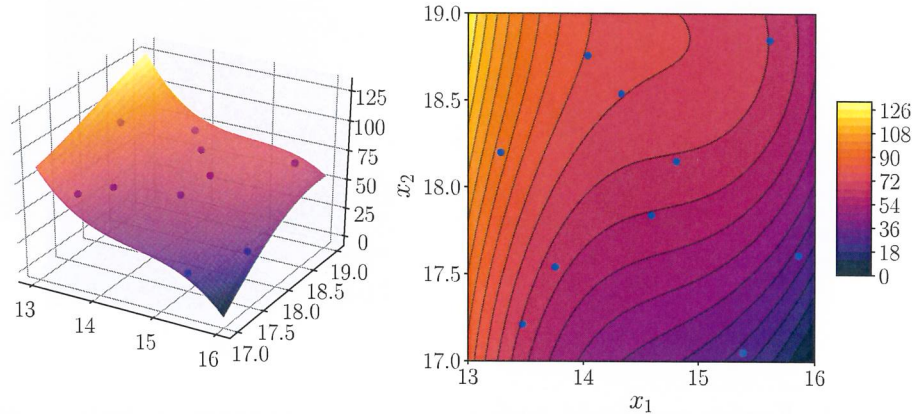


Figure 5.12: Kriging metamodel surface for using a constant trend function and the *power exponential* covariance model with parameters $\nu = 2$, $\theta = 1.895$ and $\sigma = 38.44$

It is possible to see that changing the parameters of the Kriging metamodel can change the shape of the response function, and some very bad choice of the parameters can lead to very exotic shapes like in figure 5.14. In any case it is possible to test the robustness of a certain setup using an error estimate like the one proposed in chapter 4. In practical applications the choice of the optimal parameters is usually left to the experience of the user.

Final remarks

Further detail on ~~other~~ theoretical and computational aspects can be found in Cavazzuti [38], Adams et al. [2], Sacks et al. [136] and Baudin et al. [13]. The above code snippet is public, in the GitHub repository of the author at the address: https://github.com/appanacca/kriging_book.git. The OpenTRUNS library implementation is available at the previous repository link. In addition an equivalent ordinary Kriging implementation, starting from scratch, can be downloaded. More generally whenever a reduced order model has to be built with a not extremely large amount of data the Kriging metamodeling should be a solution to investigate seriously.

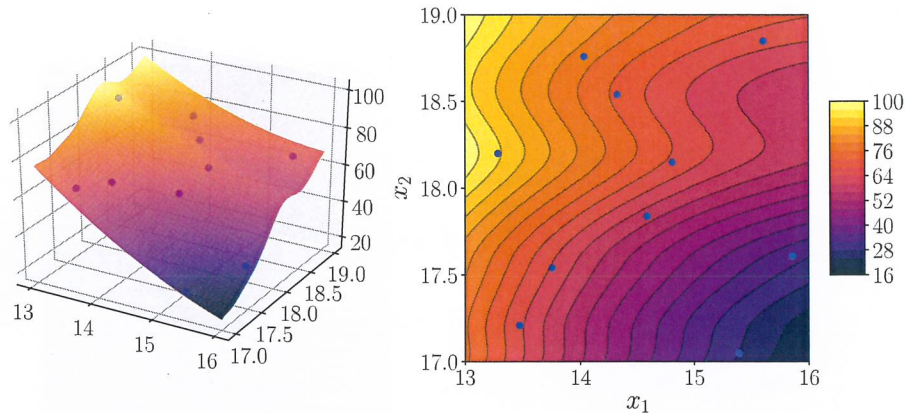


Figure 5.13: Kriging metamodel surface for using a quadratic trend function and the *Matern* covariance model with parameters $\nu = 1.5$, $\theta = 10$ and $\sigma = 1$.

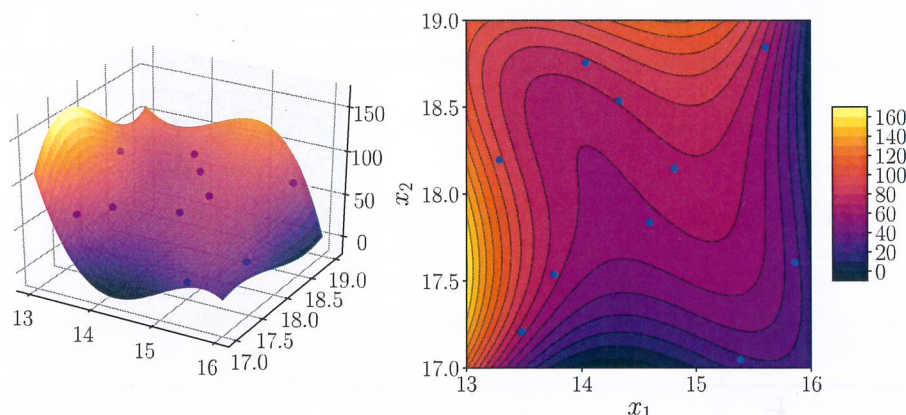


Figure 5.14: Kriging metamodel surface for using a linear trend function and the *power exponential* covariance model with parameters $\nu = 2$, $\theta = 0.8$ and $\sigma = 10$.